

3-11-2011

Analysis of Plasma Bubble Signatures in the Ionosphere

Omar A. Nava

Follow this and additional works at: <https://scholar.afit.edu/etd>

Part of the [Atmospheric Sciences Commons](#), and the [Plasma and Beam Physics Commons](#)

Recommended Citation

Nava, Omar A., "Analysis of Plasma Bubble Signatures in the Ionosphere" (2011). *Theses and Dissertations*. 1467.
<https://scholar.afit.edu/etd/1467>

This Thesis is brought to you for free and open access by the Student Graduate Works at AFIT Scholar. It has been accepted for inclusion in Theses and Dissertations by an authorized administrator of AFIT Scholar. For more information, please contact richard.mansfield@afit.edu.



**ANALYSIS OF PLASMA BUBBLE
SIGNATURES IN THE IONOSPHERE**

THESIS

Omar A. Nava, Captain, USAF
AFIT/GAP/ENP/11-M06

**DEPARTMENT OF THE AIR FORCE
AIR UNIVERSITY**

AIR FORCE INSTITUTE OF TECHNOLOGY

Wright-Patterson Air Force Base, Ohio

APPROVED FOR PUBLIC RELEASE; DISTRIBUTION UNLIMITED

The views expressed in this thesis are those of the author and do not reflect the official policy or position of the United States Air Force, the Department of Defense, or the United States Government. This material is declared a work of the U.S. Government and is not subject to copyright protection in the United States.

AFIT/GAP/ENP/11-M06

ANALYSIS OF PLASMA BUBBLE SIGNATURES IN THE IONOSPHERE

THESIS

Presented to the Faculty
Department of Engineering Physics
Graduate School of Engineering and Management
Air Force Institute of Technology
Air University
Air Education and Training Command
in Partial Fulfillment of the Requirements for the
Degree of Master of Science

Omar A. Nava, BS, MS
Captain, USAF

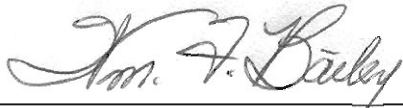
March 2011

APPROVED FOR PUBLIC RELEASE; DISTRIBUTION UNLIMITED

ANALYSIS OF PLASMA BUBBLE SIGNATURES IN THE IONOSPHERE

Omar A. Nava, BS, MS
Captain, USAF

Approved:



William F. Bailey, PhD (Chairman)

1 Mar 2011

Date



Lt Col Ariel O. Acebal (Member)

1 MAR 2011

Date



Ludger Scherliess, PhD (Member)

1 Mar 2011

Date

Abstract

Plasma bubbles are large scale structures of depleted plasma density in Earth's ionosphere that disrupt radio and satellite communications, to include global navigation satellite systems. This study used the Ionospheric Forecast Model (IFM) to analyze affected look angles and total electron content (TEC) differences due to plasma bubbles of various sizes for 27 geophysical conditions consisting of different seasons and levels of solar and geomagnetic activity at 421 GPS ground stations worldwide. Overall, different geographic locations and plasma bubble configurations produced different affected look angle profiles. Bigger plasma bubbles, larger density depletion factors, higher levels of solar activity and the equinoctial months resulted in greater slant TEC differences and, hence, greater communication problems. The results of this study not only improved the accuracy of the Air Force's operational ionospheric model and space weather forecasting capability, but also provided military leaders with a clear picture of the expected plasma bubble impacts to communications reliability when planning and executing military operations from the strategic to tactical level.

Acknowledgements

First and foremost, I would like to thank my thesis advisor, Dr. William Bailey, who guided me throughout my research with his patience and encouragement. He allowed me the freedom to explore wherever my creativity would take me. His knowledge was invaluable throughout my research and writing of this thesis. I could not have wished for a better or friendlier thesis advisor.

I would also like to thank the rest of my thesis committee. I am grateful for Lt. Col. Ariel Acebal's guidance and sense of humor throughout my thesis research. His tough classes and exams forced me to expand the boundaries of my critical thinking skills. I also learned a new way to cut watermelons and even enjoyed a stint of rare military democracy. Drs. Robert Schunk and Ludger Scherliess from Utah State University displayed a level of interest and involvement I wouldn't have expected from a team thousands of miles away. They both provided valuable insight into my research and I can't thank them enough.

Finally, I would like to thank my wife for her unending patience, love and understanding during the last 18 months at AFIT where I spent more time with my computer and books than with her. She made sure I never settled for anything less than my best work and without her constant encouragement and motivation, this thesis would not have been possible.

Omar A. Nava

Table of Contents

	Page
Abstract	iv
Acknowledgements	v
List of Figures	viii
List of Tables	x
I. Introduction	1
1.1 Background	1
1.2 Problem Statement	2
1.3 Research Objective	3
1.4 Preview	3
II. Literature Review	4
2.1 Ionosphere	4
2.2 Earth's Magnetic Field	5
2.2.1 Dipole Magnetic Field	6
2.2.2 World Magnetic Model (WMM)	8
2.3 Plasma Bubbles	9
2.3.1 Rayleigh-Taylor Instability	9
2.3.2 Plasma Bubble Characteristics	11
2.4 Scintillation	15
2.5 Modeling the Ionosphere	16
2.5.1 Ionospheric Forecast Model (IFM)	16
2.5.2 Global Assimilation of Ionospheric Measurements (GAIM) Model	18
III. Methodology	20
3.1 Geophysical Conditions	20
3.2 Modeling with the IFM	21
3.2.1 Plasma Bubble Structure	21
3.2.2 Geomagnetic Equator	23
3.2.3 Plasma Bubble Alignment	24
3.3 Development of Utilities	27
3.4 Look Angle Analysis	29
3.5 Slant TEC Analysis	32
3.6 Plasma Bubble Occurrence Statistics	36

	Page
IV. Results and Analysis	38
4.1 Look Angle Analysis	38
4.1.1 Look Angle Profiles	38
4.1.2 Time Evolution	45
4.2 Slant Total Electron Content Analysis	50
4.2.1 Bubble Configuration Comparison	52
4.2.2 Season	54
4.2.3 Solar Activity	56
4.2.4 Geomagnetic Activity	56
V. Discussion	61
5.1 Look Angle Analysis	61
5.2 Slant TEC Analysis	62
5.3 Further Study	63
5.3.1 Singapore University Research Collaboration	63
5.3.2 Scintillation Network Decision Aid (SCINDA) Data	64
5.4 Conclusion	65
Bibliography	67
Vita	69

List of Figures

Figure	Page
1. Ionosphere Profile	5
2. Dipole Magnetic Field	7
3. Airglow Imagery	10
4. Rayleigh-Taylor Instability	11
5. Plasma Bubble Structure	12
6. Plasma Bubble Occurrence Statistics	14
7. GPS Radio Wave Scintillations and TEC Variations	17
8. Plasma Bubble Outlines	22
9. Embedded Plasma Bubble in the IFM Output	23
10. Plasma Bubble Alignment Process	25
11. Plasma Bubbles Aligned With Earth's Magnetic Field	26
12. Bubble Depletion Width	29
13. GPS Ground Station Grids	31
14. Look Angle Analysis Flow Diagram	33
15. Slant TEC Analysis GPS Satellite Positions	34
16. Slant TEC Analysis Flow Diagram	35
17. Analysis Regions	37
18. Affected Look Angle Profiles	39
19. Affected Look Angle vs. Plasma Bubble Size	41
20. Affected Look Angles vs. Distance from Geomagnetic Equator	42
21. Look Angle Asymmetry	44

Figure	Page
22. Look Angle Asymmetry Depiction	44
23. Affected Look Angle vs. Region (Geomagnetic Equator)	46
24. Affected Look Angle vs. Region (North of Geomagnetic Equator)	47
25. Affected Look Angle vs. Time	49
26. Vertical TEC vs. Season	51
27. Slant TEC Difference	53
28. Geophysical Condition Comparison - Season	55
29. Geophysical Condition Comparison - Solar Activity	57
30. Vertical TEC vs. Geomagnetic Activity	58
31. Geomagnetic Activity TEC Difference Comparison	60
32. Affected GPS Ground Stations vs. Plasma Bubble Size	66

List of Tables

Table		Page
1.	World Magnetic Model Input and Output Parameters	8
2.	Plasma Bubble Characteristics	15
3.	Geophysical Conditions	20
4.	Plasma Bubble Configurations	21
5.	MATLAB Utilities	28
6.	Analysis Regions	36
7.	Slant TEC Analysis Bubble Configurations	52

I. Introduction

1.1 Background

Plasma bubbles are large scale structures of depleted plasma density in Earth's ionosphere that affect communication signals propagating through the atmosphere. The irregular plasma density gradients force radio and satellite communication signals to fluctuate wildly in both phase and amplitude, often resulting in a loss of signal lock. Because GPS has been incorporated into many different types of military weapon systems ranging from GPS guided munitions to hand-held receivers that enable soldiers to quickly navigate streets of foreign cities, ignorance of plasma bubbles may have devastating and even deadly consequences.

Besides crippling communication and precision engagement capabilities, plasma bubbles can also degrade Intelligence, Surveillance and Reconnaissance (ISR) operations, resulting in miscalculated enemy positions and misidentified space objects and orbit tracks. Errors in orbital positions could result in disastrous collisions with satellites, the International Space Station or the Space Shuttle. Because the presence of plasma bubbles can jeopardize the success of military operations, damage or debilitate military assets and capabilities, and endanger military and civilian lives, it is imperative that military leaders be knowledgeable of plasma bubbles and their impacts on radio and satellite communications reliability.

1.2 Problem Statement

This research addresses two problems, one operational and the other computational. Operationally, it is important for military leaders to know when and where plasma bubbles will occur and the extent of their impact on radio and satellite communications when planning and executing military operations. By characterizing the affected look angles and electron density differences for a wide range of geophysical conditions and plasma bubble configurations, communication problems can be forecast, giving commanders the knowledge to make decisions necessary to ensure mission success.

Computationally, the operational Air Force ionospheric model at the Air Force Weather Agency (AFWA) is the Gauss-Markov Global Assimilation of Ionospheric Measurements (GAIM-GM) model developed by a team at Utah State University (USU). The operational GAIM model uses the Ionospheric Forecast Model (IFM) as its physics-based model. A new Full Physics GAIM (GAIM-FP) model, currently in development by the USU team, incorporates the Ionosphere-Plasmasphere Model (IPM). Neither ionospheric model includes the physics necessary to allow for the consistent self-excitation of plasma bubbles structures. As a result, plasma bubbles will cause the models to incorrectly reconstruct Earth's ionosphere, creating widespread regions of low electron densities where the bubbles were located. In GAIM-FP, the self-consistent electric fields and neutral winds deduced by the model will also be incorrect [20]. Characterizing the affected look angles will alert users that the ionospheric model output at certain geographic locations may be suspect due to the presence of plasma bubbles. In addition, if GPS data influenced by plasma bubbles is prevented from being ingested into the GAIM model, the accuracy of the model output will be increased.

1.3 Research Objective

The research objective is to create an archive of affected look angles and total electron content (TEC) differences due to plasma bubbles of various sizes for 27 geographical conditions consisting of different seasons, levels of solar activity and levels of geomagnetic activity at 421 GPS ground stations worldwide using the Ionospheric Forecast Model (IFM). The results of the study will not only improve the accuracy of the Air Force's operational ionospheric model and space weather forecasting capability, but also provide military leaders with a clear picture of the expected plasma bubble impacts to communications reliability when planning and executing military operations from the strategic to tactical level.

1.4 Preview

The following chapters will provide details about the research. Chapter 2 will present background information on Earth's ionosphere and magnetic field, plasma bubble formation and characteristics, scintillation, and two ionospheric models: IFM and GAIM. Next, Chapter 3 will provide an overview of the methodology used in this study to include modeling plasma bubble structures using the IFM, development of the analysis utilities and a description of the look angle and slant TEC calculation algorithms. The results of the look angle and slant TEC analyses will be presented in Chapter 4. Lastly, Chapter 5 will provide some insight into the results and suggest topics for further study.

II. Literature Review

This chapter will provide some background information on topics pertinent to this research. First, the Earth's ionosphere will be described because plasma bubbles form in this region of the upper atmosphere. Information about Earth's magnetic field will be presented since plasma bubbles elongate along magnetic field lines. Next, plasma bubbles will be elaborated in detail since their characteristics are necessary to accurately model their structure and movement. Scintillation and its effect on satellite communications and GPS will be also discussed. Lastly, two different ionospheric models, the IFM and GAIM, will be described.

2.1 Ionosphere

The ionosphere is a region in Earth's upper atmosphere where significant numbers of free thermal electrons and ions are present. Processes involved in the creation of the ionosphere are photoionization by solar extreme ultraviolet (EUV) and x-ray photons, and impact ionization by charged particles, to include solar and galactic cosmic rays. Photoionization is the dominant ionization process during the daytime at equatorial and subauroral latitudes while impact ionization by precipitating auroral electrons plays an important role at high latitudes at night. Once the free electrons and ions are formed, they are affected by several production and loss processes including chemical reactions, diffusion, wave disturbances, plasma instabilities and transport due to electric and magnetic fields and neutral winds [18].

The ionosphere begins at about 60 km and extends beyond 1000 km. The layers of the ionosphere and the principle ions that compose each region are presented in Figure 1. The ionosphere is structured vertically in three regions that differ in composition, density, ionization sources, degree of variability, chemistry and dynamics: D region,

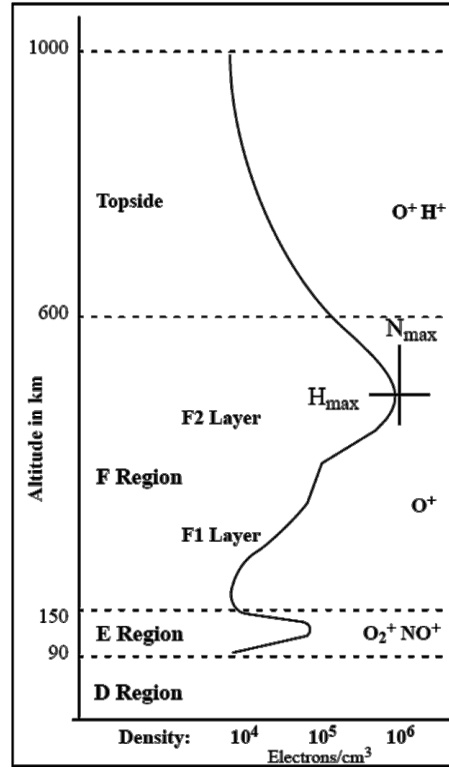


Figure 1. Depiction of the different layers of Earth's ionosphere. Adapted from Anderson and Rowell.

E region, and F region. Above the F region is a layer known as the topside ionosphere where exponentially decreasing plasma densities extend vertically to a few thousand kilometers. The maximum ionospheric plasma density occurs in the F region around 300 km. At night, ionospheric densities can decrease up to two orders of magnitude depending on the ionospheric region and altitude. The largest decay occurs in the D and E regions due to recombination between molecular ions and free electrons. Overall, plasma densities in the ionosphere vary with season, time of day, solar cycle and level of geomagnetic activity [18].

2.2 Earth's Magnetic Field

Earth's magnetic field is generated by a combination of three main sources: Earth's conducting fluid outer core, the crust and upper mantle, and electrical currents flow-

ing in the upper atmosphere and magnetosphere. The observed magnetic field, as measured by a magnetic sensor on or above Earth's surface, is dominated by Earth's main magnetic field (conducting, fluid outer core), accounting for over 95% of the field strength [9]. The next sections will describe methods of representing and modeling Earth's magnetic field.

2.2.1 Dipole Magnetic Field

The simplest way to represent Earth's magnetic field is through a dipole approximation illustrated in Figure 2. Mathematically, if \mathbf{m} is the dipole moment at the Earth's center, then the magnetic scalar potential (Φ_m) is given by

$$\Phi_m(r, \theta, \phi) = \frac{m \cos \theta}{r^2}. \quad (1)$$

By taking the gradient of the scalar potential, the magnetic field (\mathbf{B}) is equal to

$$\mathbf{B} = -\nabla \Phi_m = \frac{2m \cos \theta}{r^3} \mathbf{e}_r + \frac{m \sin \theta}{r^3} \mathbf{e}_\theta \quad (2)$$

where \mathbf{e}_r and \mathbf{e}_θ are unit vectors in the radial and polar directions, respectively [18].

The equation used to model the dipole field line in Figure 2 is obtained from the expression

$$\frac{r d\theta}{dr} = \frac{B_\theta}{B_r} = \frac{\tan \theta}{2} \quad (3)$$

which relates differential arc lengths in the spherical coordinate system to the magnetic field components described in Equation 2 [18]. The solution to Equation 3 relating the dipole field line radius r to the colatitude θ is

$$r = R_0 \sin^2 \theta \quad (4)$$

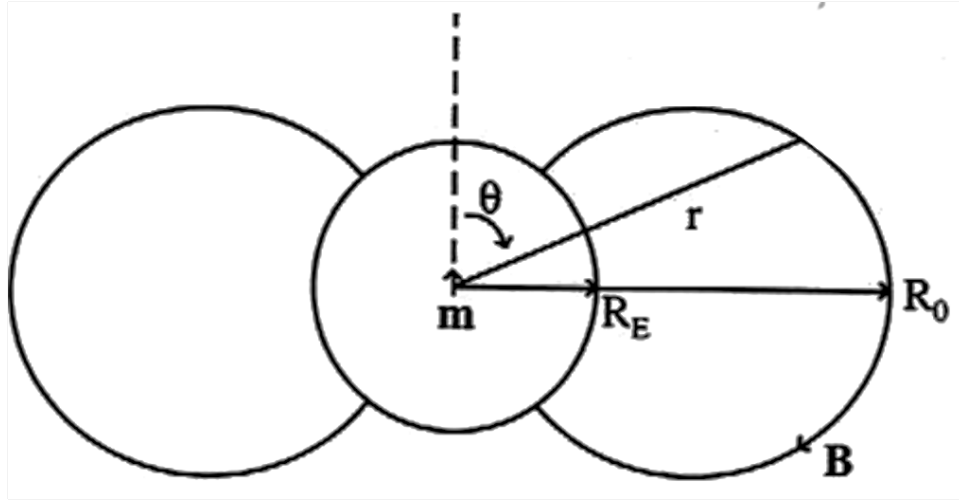


Figure 2. Parameters used to describe a magnetic dipole field line. Adapted from Schunk and Nagy.

where R_0 is the radial distance to the point where the dipole field crosses the geomagnetic equator. The magnetic dipole is a reasonable approximation for the magnetic field at low and middle latitudes [18].

Two commonly used angles to describe the Earth's magnetic field are the declination and inclination angles. The declination angle is the deflection of the magnetic field from the geographic pole. When the declination angle is equal to zero, the magnetic field is in the same direction as the geographic pole. The inclination angle or dip angle of the magnetic field is a measure of the deviation from the horizontal, which is parallel to the Earth's surface. When the inclination angle is equal to zero, the magnetic field is parallel to the Earth's surface and is defined as the geomagnetic equator. Magnetic declination and inclination angles are not uniform over the Earth's surface. The largest declination angles are located close to the magnetic poles and, because the geographic and geomagnetic poles are not co-located, the geographic equator does not run parallel with the geomagnetic equator [18].

2.2.2 World Magnetic Model (WMM)

The World Magnetic Model (WMM) is another method of modeling the Earth's magnetic field. The WMM is a joint product of the United States' National Geospatial-Intelligence Agency (NGA) and the United Kingdom's Defence Geographic Centre (DGC) [9]. It is the standard model used by the U.S. Department of Defense, the U.K. Ministry of Defence, the North Atlantic Treaty Organization (NATO) and the International Hydrographic Organization (IHO), for navigation, attitude and heading referencing systems using the magnetic field. It is also used widely in civilian navigation and heading systems [9]. The WMM consists of a degree and order 12 spherical-harmonic main field model comprised of 168 spherical-harmonic Gauss coefficients and a degree and order 12 spherical-harmonic Secular-Variation (SV) field model to calculate changes to the magnetic field over time [9]. The input and output parameters for the WMM are detailed in Table 1.

Table 1. World Magnetic Model Input and Output Parameters

Input Parameter	Range
Latitude	-90.00 to +90.00 degrees
Longitude	-180.00 to +180.00 degrees
Altitude	Sea level to 1000 km (referenced to the WGS 84 ellipsoid)
Date Base	Epoch of the current model to epoch + 5 years
Output Parameter	Definition
B	Total Intensity
H	Horizontal Intensity
X	North Component
Y	East Component
Z	Vertical Component
I (DIP)	Geomagnetic Inclination
D (DEC)	Geomagnetic Declination (Magnetic Variation)

2.3 Plasma Bubbles

Plasma bubbles, also called equatorial plasma bubbles (EPBs) or plasma depletions, are large-scale structures of reduced F region plasma densities that first appear at the bottomside of the F layer (200 km) and extend vertically into the topside of the ionosphere. Because these phenomena are similar to bubbles rising through a liquid, they are called plasma bubbles [13]. Plasma bubbles have been studied for decades using different techniques including incoherent backscatter radar, ionogram analysis, airglow detection, rocket soundings, in situ satellite measurements and GPS network phase fluctuations [14]. Plasma bubbles observed using 630.0-nm airglow optical imagery are shown in Figure 3.

However, many of the aforementioned methods have severe limitations. Coherent scatter radar detects only highly localized irregularities and airglow detection is hampered by the presence of clouds or moonlight. In contrast, the GPS network allows continuous monitoring of the generation and evolution of plasma bubbles on a large scale due to its permanent operation and near global coverage [14].

2.3.1 Rayleigh-Taylor Instability

Plasma bubble formation can be explained through a discussion of the Rayleigh-Taylor Instability (RTI) configuration depicted in Figure 4. The diagram shows that on the geomagnetic equator, Earth's magnetic field lines are oriented horizontally towards geomagnetic north and the F region plasma has a uniform density distribution along the field line due to diffusion. The gravitational force acting upon the electrons and ions results in an external force drift, generating an eastward electric current. If a small density fluctuation is produced on the bottomside of the ionosphere (e.g. by gravity waves) the isodensity surface will undulate. The electrons and ions become separated, resulting in a local buildup of positive and negative charges. Since ions

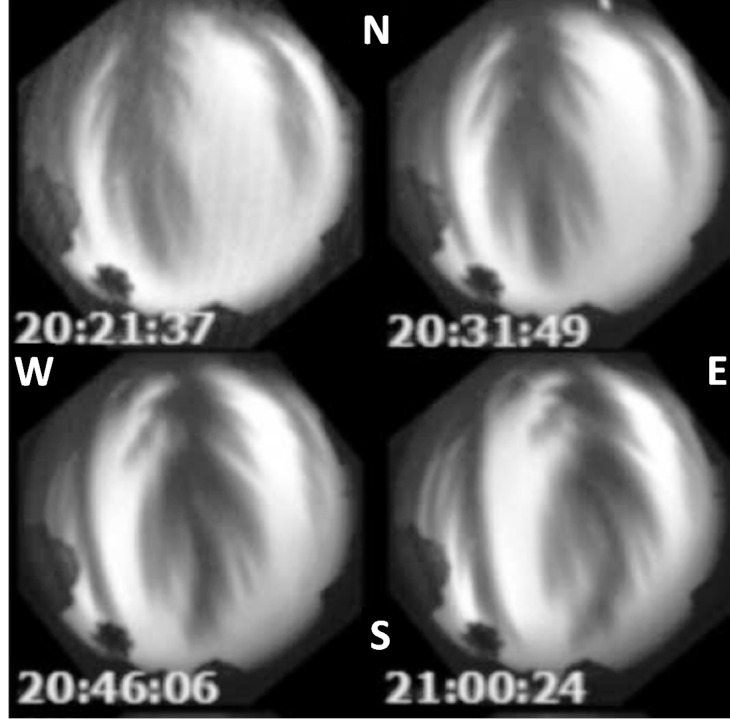


Figure 3. Sequence of 630.0-nm emission all-sky optical images showing the evolution and spatial characteristics of equatorial plasma bubbles. Adapted from Abalde et al.

carry the electric current, the resulting localized polarization electric fields will have eastward orientations in the low-density regions and westward orientations in the high-density regions. Consequently, the $E \times B$ drift due to this polarization field will be upward in the low-density region and downward in the high-density region. The amplification of the density fluctuations leads to the formation of plasma bubbles [8].

Mathematically, the growth rate (γ) of plasma bubbles due to RTI is described by the equation

$$\gamma = -\frac{g}{v_{in}} \frac{1}{n_{i0}} \frac{\partial n_{i0}}{\partial y} \quad (5)$$

where g is the acceleration due to gravity, v_{in} the ion-neutral collision frequency, and n_{i0} the background electron density [8]. The equation indicates that when the gravitational force and the electron density gradient are anti-parallel (on the bottomside of the ionosphere) the growth rate is positive and the magnitude is proportional to the

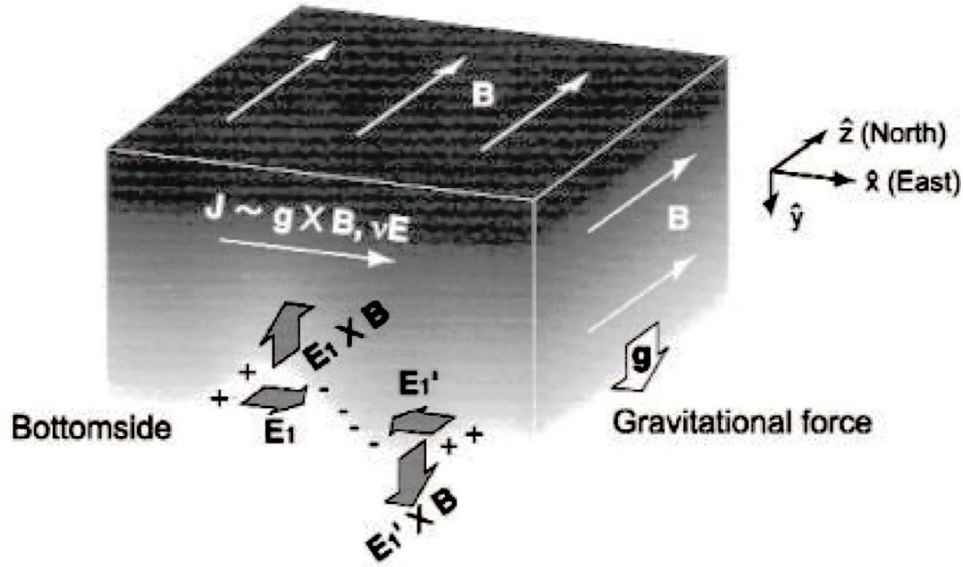


Figure 4. Rayleigh-Taylor Instability configuration. Adapted from Maruyama.

density gradient. After sunset, the rapid decrease in electron density on the bottomside of the ionosphere increases the density gradient and, therefore, the growth rate [8]. Furthermore, since the ion-neutral atmospheric particle collision frequency (v_{in}) decreases with height, growth conditions are further enhanced [13]. In contrast, since the density gradient reverses above the F region peak, fluctuations will not continue to grow in amplitude and the ionosphere will become stable. Because the increase in growth rate only occurs after sunset, plasma bubbles are essentially a nighttime phenomenon. Instabilities can also develop in a similar manner for electric currents generated by means other than gravity [8].

2.3.2 Plasma Bubble Characteristics

The typical plasma bubble configuration, depicted in Figure 5, shows that the plasma density depletions diffuse along the Earth's magnetic field lines [17]. The depleted regions take the form of vertically elongated wedges of depleted plasma resembling upside down watermelon slices with an apex height determined by the

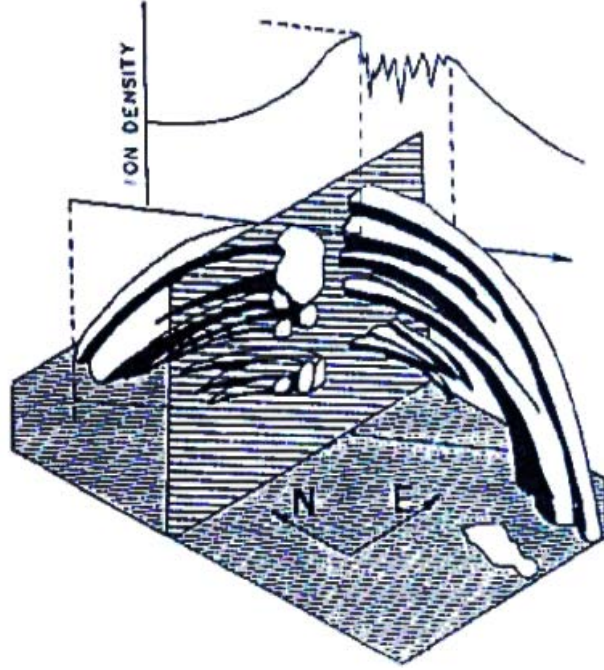


Figure 5. Plasma bubble structure showing that plasma density depletions elongate along dipolar field lines. Adapted from Young et al.

dipole field line. Plasma bubbles have density depletions of about a factor of 10, but factors of 100 and 1000 are also fairly common [17]. In addition, plasma bubble regions having a high degree of depletion are observed to be associated with larger depletion widths, since deeper depletions extents are associated with well developed irregularities with large amplitudes. Shallower depletions are associated with weaker irregularities in their formation stages [22].

Plasma bubbles also vary greatly in size. Coherent scatter radars at Jicamarca, Peru and Kwajalein, Marshall Islands respond to plasma density irregularities of meter scale sizes [4]. Furthermore, plasma density depletions detected by Atmosphere Explorer E (AE-E) and Defense Meteorological Satellites Program (DMSP) satellites showed longitudinal scale sizes of tens of kilometers [4]. It was also discovered that plasma bubbles can extend vertically to altitudes greater than 1500 km [15]. The tilt of plasma bubbles ranges from 10 to 15 degrees toward the west relative to the

Earth's magnetic field, suggesting that they may be associated with the variation of plasma drifts with altitudes [22]. The interdepletion distance (IDD) or horizontal distance between separate depleted density regions can range from 400 to 1600 km, varying due to geomagnetic storming [22].

Plasma bubbles typically drift upward with velocities varying between 100 and 500 meters per second (m/s), but "fast bubbles" with velocities between 500 m/s and 5 km/s occur fairly often as well [18]. In the horizontal direction, plasma bubble drift velocities were observed to range between 40 and 190 m/s towards the east. Drift velocities were highest (190 m/s) around 2100 local time (LT) and showed a gradual decrease to about 40 m/s by 0100 LT before the depletion became extremely weak [22]. Plasma bubble generation typically starts at 2000 LT (after sunset) and usually ends by 0100 LT [7]. After plasma bubble generation has ceased, some bubbles corotate with the Earth while other plasma bubbles have also been observed to superrotate with speeds up to 3 km/s [17]. Around 0600 LT, the plasma bubbles dissipate due to increased ionization associated with sunrise.

Plasma bubble occurrence statistics are presented in Figure 6 as a function of solar activity, season and geographic region between 2000 and 2006. The histogram indicates that more plasma bubbles were detected during solar maximum (2000) when compared to solar minimum (2006) [10]. It was also observed that during solar maximum, plasma bubbles reached apex heights over 1500 km more often [15]. In addition, each geographic region displays different months of peak plasma bubble formation due to a magnetic declination dependence [8].

Finally, it was observed that conditions conducive to the growth of deep plasma bubbles were enhanced during high geomagnetic activity [4]. During the early part of geomagnetic storming, intense plasma bubble activity was almost always detected and the onset of formation was typically delayed in the pre-midnight sector [7]. In-

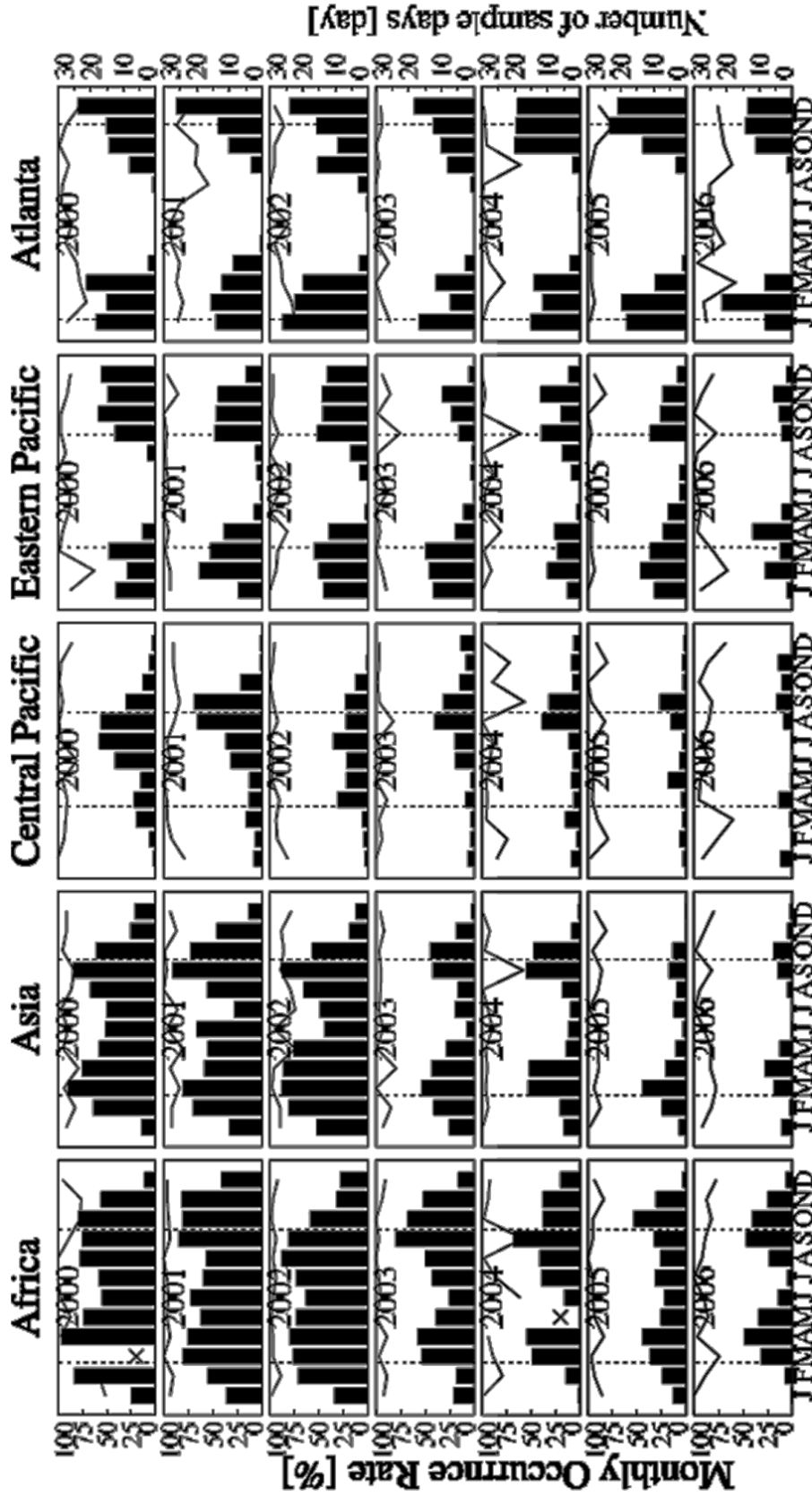


Figure 6. Monthly occurrence rates of plasma bubbles from 2000 to 2006. The histogram shows the occurrence rate with the scale on the left-hand side of the plot. The averaged number of sample days (continuous line) are displayed with the scale on the right-hand side. Adapted from Nishioka et al.

stead of commencing at 2000 LT during quiet geomagnetic conditions, plasma bubble generation did not begin until after midnight. For several days after the beginning of a storm's recovery phase, it was also discovered there was a near-total absence of plasma bubbles [4]. A summary of the plasma bubble characteristics is presented in Table 2.

2.4 Scintillation

One of the first known impacts on radio signals transmitted through the Earth's ionosphere was rapid amplitude and phase fluctuations due to an effect known as scintillation. Ionospheric scintillation causes signal quality degradation and even loss of signal reception or signal lock if amplitude fluctuations are severe. GPS receivers unable to receive and track GPS satellite signals may experience navigation errors or even navigation failure. The strength of the amplitude scintillations is quantified by a metric called the S_4 index. The S_4 index is the ratio of the standard deviation of the signal power to the mean signal power computed over a period of time, which is

Table 2. Plasma Bubble Characteristics

Characteristic	Typical Values	Source
Depletion Extent	10x, 100x, 1000x	[18],[22]
N-S Extent	Several thousands of km	[15]
Width	Several hundred km	[15]
Apex Height	≥ 1500 km	[18],[15],[21]
IDD	400 to 800 km (quiet) 1600 km (active)	[22] [22]
Start Time	2000 LT (quiet) 2400 LT (storming)	[7] [7]
End Time	0100 LT	[22],[18]
Dissipation Time	0600 LT (sunrise)	
Upward Drift	100 to 500 m/s (slow) 500 m/s to 5 km/s (fast)	[18] [18]
Eastward Drift	40-190 m/s	[22]
Tilt	10-15 deg to the west	[22]

$$S_4 = \sqrt{\frac{\langle I^2 \rangle - \langle I \rangle^2}{\langle I \rangle^2}} \quad (6)$$

where I is the signal intensity averaged over a time period of 60 seconds [6].

Ionospheric scintillations occur when radio signals propagate through an irregular ionosphere; for example, total electron content (TEC) gradients associated with plasma bubbles. TEC is a measure of the number of electrons in a volume with a one meter-squared (m^2) cross section and length equal to the signal path. It is typically expressed in TEC units (TECU) with one TECU equal to 10^{16} electrons/ m^2 [6]. Since plasma bubbles are regions of depleted ion and electron densities, a plasma bubble located on the satellite-to-ground signal path will cause radio signals to fluctuate in phase and amplitude. TEC measurements from a GPS satellite transmitting through a plasma bubble region are depicted in Figure 7. When GPS satellite PRN 14 transmits through the plasma bubble region shortly after 2200 LT, the radio signal power fluctuates rapidly and the TEC decreases sharply. After the GPS satellite exits the plasma bubble region around 2330 LT, the signal power stabilizes and the TEC curve becomes smoother.

2.5 Modeling the Ionosphere

This section will describe two different ionospheric models: the IFM and GAIM. The IFM was used to create global electron density maps into which plasma bubbles were embedded. The GAIM model has been the current operational Air Force ionospheric model at the Air Force Weather Agency (AFWA) since 2006 [23].

2.5.1 Ionospheric Forecast Model (IFM)

The IFM is a physics-based numerical model of the global ionosphere. The IFM calculates three-dimensional, time-dependent density distributions for four major ions

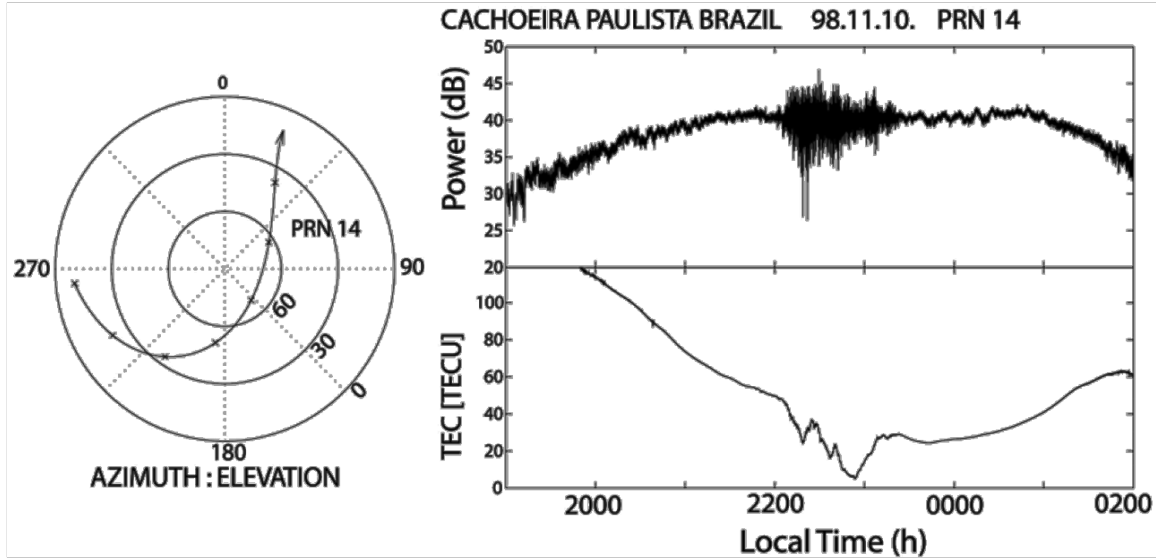


Figure 7. The left figure depicts the relative positions of GPS satellite PRN 14 to the GPS ground station in terms of azimuth and elevation angles over time. The figure on the right shows amplitude scintillations and TEC variations associated with GPS signal propagation through a plasma bubble. Adapted from Kintner et al.

(NO^+ , O_2^+ , N_2^+ , O^+) at E region altitudes, two major (O^+ , NO^+) and two minor (N_2^+ , O_2^+) ions at F region altitudes, and ion and electron temperatures at both E and F region altitudes. The IFM also calculates H^+ densities in the F region and topside ionosphere. The model covers altitudes from 90 to 1600 km, and outputs density values at a spatial resolution of 4 km in the E region and 20 km in the F region. The model outputs the density and temperature distributions in either a geographic or geomagnetic coordinate system with a 3° latitude-resolution and 7.5° longitude resolution. The IFM's model drivers include F10.7, year, day, start time, duration of the model run and the temporal variation of Kp from 3 hours prior to the start time through the end of the simulation [19].

The IFM is based on a numerical solution of the ion and electron continuity, momentum, and energy equations and accounts for the following physical processes: (1) field-aligned diffusion due to density and temperature gradients, gravity, and the ambipolar electric field; (2) cross-field electrodynamic drifts due to both magneto-

spheric and dynamo electric fields; (3) ion production due to UV and EUV solar radiation, scattered solar radiation, starlight, and auroral electron precipitation; (4) numerous energy-dependent chemical reactions; (5) thermospheric winds; (6) neutral composition changes; (7) thermal conduction; and (8) a myriad of elastic and inelastic heating and cooling processes. The IFM also takes account of the offset between the geomagnetic and geographic poles [19].

2.5.2 Global Assimilation of Ionospheric Measurements (GAIM) Model

GAIM is a physics-based data assimilation model of Earth's ionosphere and neutral atmosphere developed by a team at Utah State University (USU) that uses a time-dependent physics-based model of the global ionosphere-plasmasphere and a Kalman filter as a basis for assimilating a diverse set of real-time (or near real-time) measurements. The operational Air Force ionospheric model at the Air Force Weather Agency (AFWA) is the Gauss-Markov Global Assimilation of Ionospheric Measurements (GAIM-GM) model which uses the Ionospheric Forecast Model (IFM) as its physics-based model. A new Full Physics GAIM (GAIM-FP) model is currently in development by the USU team that incorporates the Ionosphere-Plasmasphere Model (IPM). GAIM is able to provide both specifications and forecasts on a spatial grid that can be global, regional or local (25 km x 25 km). The primary output of GAIM is a continuous reconstruction of the three-dimensional electron density (Ne) distribution from 90 km to 35,000 km (geosynchronous altitude). The model also outputs auxiliary parameters, including $N_m F_2$, $h_m F_2$, $N_m E$, $h_m E$, and slant and vertical TEC. Furthermore, GAIM provides global distributions for the ionosphere drivers (neutral winds and densities, magnetospheric and equatorial electric fields, and electron precipitation patterns). In its specification mode, GAIM provides an estimation of the amount of error in the reconstructed ionospheric densities [19].

GAIM also has the ability to assimilate a wide range of data types from numerous ground-based locations and space-based platforms. Data sources include the following: 1) In situ electron densities from National Oceanic and Atmospheric Administration (NOAA) and Department of Defense (DoD) operational satellites, 2) bottomside electron density profiles from a network of 100 Digisondes, 3) line-of-sight TEC measurements between as many as several thousand ground stations and the GPS satellites, 4) TECs between low-altitude satellites with radio beacons and several ground-based tomography chains, 5) TECs via occultations between various low-altitude satellites and between low- and high-altitude satellites, and 6) line-of-sight UV emission data. Because GAIM has a modular construction, when new models, observing stations and data types become available, they can be easily incorporated into the data assimilation scheme [19].

This chapter provided background information on several important topics relevant to this research. The next chapter will present the methodology of building the plasma bubble configurations and placing them in the IFM. The algorithms used to calculate affected look angles and slant TEC differences will also be described.

III. Methodology

This chapter will describe the methodology used in conducting the research. The first section will characterize the electron density maps for different geophysical conditions created using the IFM. The following sections will detail how plasma bubbles were embedded into the IFM electron density maps. Next, the look angle and slant TEC analysis algorithms will be described and the final section will illustrate how the plasma bubble occurrence statistics in the literature were used to analyze the results.

3.1 Geophysical Conditions

First, global electron density maps were created using the IFM. Three different seasons, solar activity levels and geomagnetic activity levels, outlined in Table 3, were combined to form 27 different geophysical conditions that were explored in this research. The IFM electron density maps were created hourly for a period of 24 hours, resulting in 24 maps for each of the 27 geophysical conditions, totaling 648 different maps. It should be noted that only Fall equinox (Day 267) was considered in this study instead of Spring equinox. Even though the plasma bubble occurrence statistics in Figure 6 indicate that there are slightly different plasma bubble occurrence rates between the two equinoctial seasons, the plasma density distribution associated with equinox was the only concern for the purposes of calculating slant TEC. Lastly, all geomagnetic activity began at 0000 UT and continued for a period of 24 hours.

Table 3. Geophysical Conditions

Season (Day)	Solar Activity (F10.7)	Geomagnetic Activity (Kp/Ap)
Summer (175)	75	1/4
Equinox (267)	150	5/48
Winter (358)	225	9/400

3.2 Modeling with the IFM

Having identified the geophysical conditions to be explored, the process of building the plasma bubble structures will be described in detail followed by the procedures of placing them into the IFM electron density maps and aligning them along the Earth's magnetic field lines. Before the plasma bubbles were constructed, the original distance between latitudinal and longitudinal IFM grid points was decreased to 3.75 degrees and 1.5 degrees, respectively, and the variable spacing between altitude grid points was halved. The smaller longitudinal width enabled the plasma bubbles to be modeled more accurately and realistically. The electron densities were linearly interpolated to determine their values at the new IFM grid points.

3.2.1 Plasma Bubble Structure

Because plasma bubbles are elongated along the Earth's magnetic field lines, the plasma bubble structure will parallel the dipole field line structure. Using the relationship between the dipole magnetic field line radius and colatitude in Equation 4, the base extent of the plasma bubble, measured at 200 km, is the only parameter necessary to define the apex height and shape of the depleted density region. The 15 different plasma bubble configurations analyzed in the study are listed in Table 4. Note that there are only five different plasma bubble sizes. Each size will be analyzed using three different depletion factors, resulting in a total of 15 different plasma

Table 4. Plasma Bubble Configurations

Base Extent (Apex Height)	Depletion Factor
3000 km (446 km)	10, 100, 1000
3500 km (622 km)	10, 100, 1000
4000 km (814 km)	10, 100, 1000
4500 km (1054 km)	10, 100, 1000
5000 km (1358 km)	10, 100, 1000

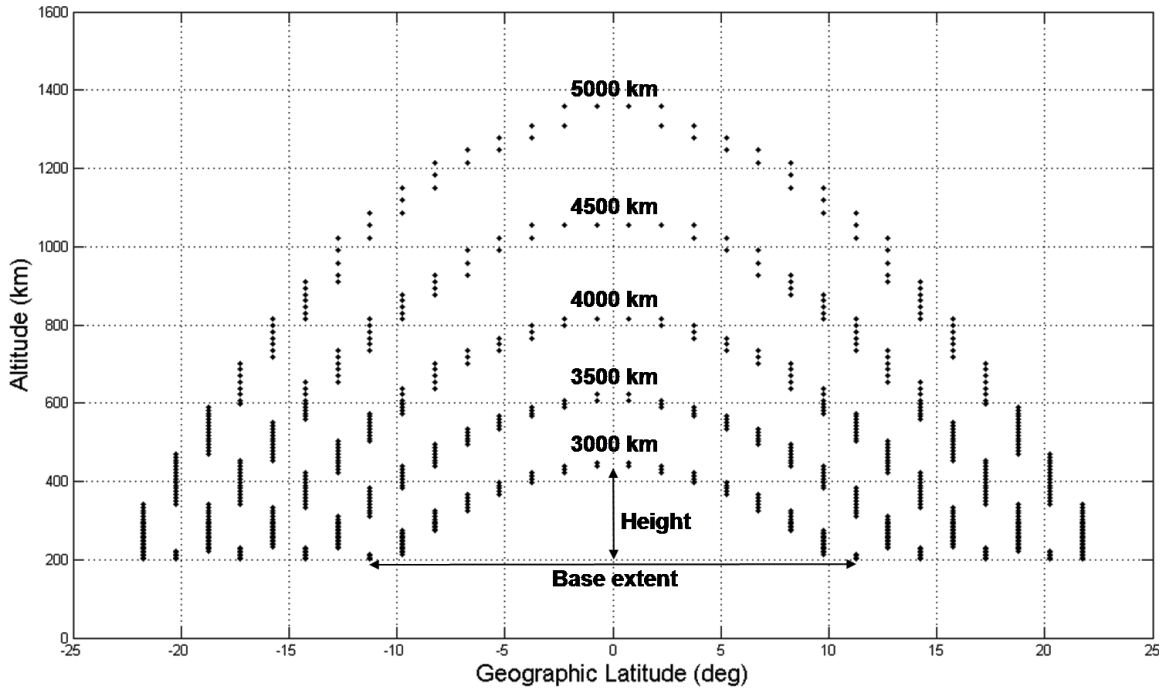


Figure 8. Outlines of the five different plasma bubble sizes embedded into the IFM electron density grid plotted as a function of altitude and geographic latitude.

bubble configurations. The five plasma bubble sizes are illustrated in Figure 8.

Next, the plasma bubbles were placed in the IFM by dividing the electron density at each plasma bubble grid point by a specified depletion factor of 10, 100 or 1000. A longitude cross section of a plasma bubble of 4000 km base extent embedded in the IFM electron density grid is presented in Figure 9. Because of the coarse latitude grid resolution, the plasma bubble outline exhibits a stair-step pattern, instead of a smooth curve. In addition, the ability to model the 10-15 degree westward tilt of the plasma bubbles is limited. A 15 degree westward tilt for the maximum plasma bubble height used in this study (1358 km) would result in a longitudinal difference of 351 km, which cannot be resolved by the grid resolution. For the purposes and scale of this study, this limitation is not important and will have minimal consequences on the affected look angle and slant TEC calculations.

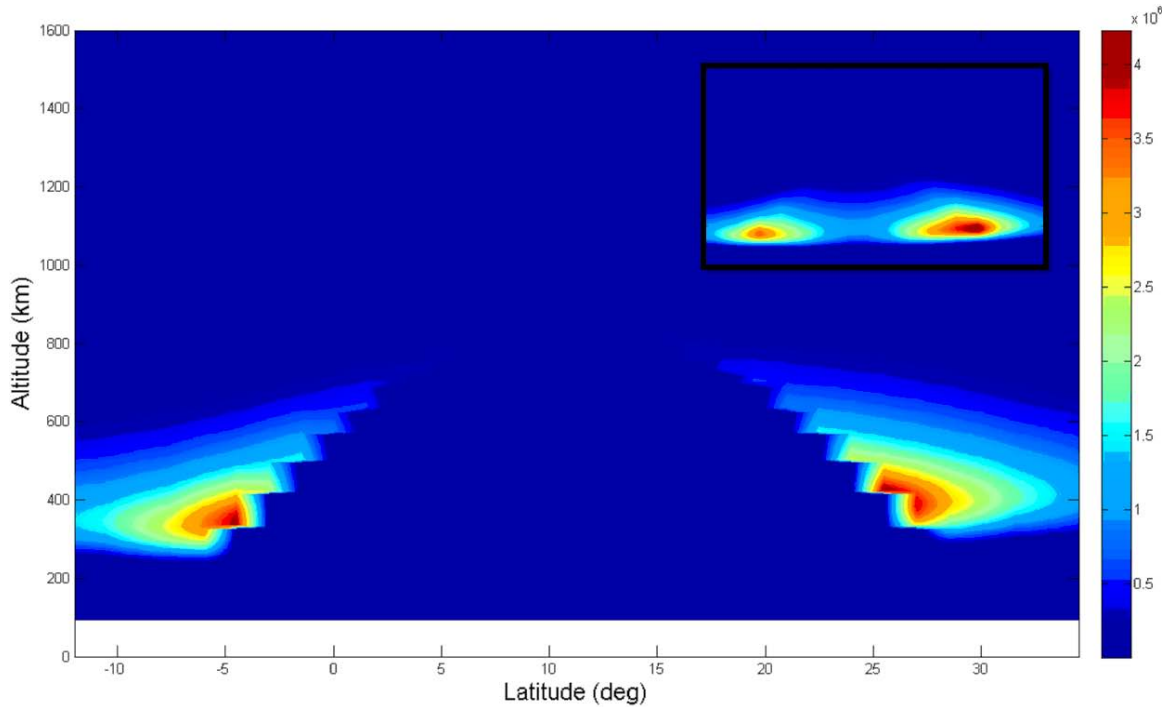


Figure 9. Longitude cross section of a plasma bubble with 4000 km base extent and depletion factor of 1000 embedded in the IFM. The inset shows the original undepleted IFM electron density. The electron density scale on the right side of the figure ranges from 0 to 4.5×10^6 electrons/cm³.

3.2.2 Geomagnetic Equator

After creating the plasma bubble structures in the IFM electron density maps, MATLAB's WMM function, described in Section 2.2.2, was used to center the bubbles on the geomagnetic equator. For each geographic longitude, the geographic latitude where the dip or inclination angle was closest to zero was determined to be the location of the geomagnetic equator. Rounding that location to the nearest IFM latitude grid point enabled the plasma bubbles to be embedded directly onto the electron density grid, eliminating the need for more complicated interpolation. Because of the 1.5 degree latitude spacing, a maximum error of 0.75 degrees latitude (83 km) is inherent in the position of the geomagnetic equator at each geographic longitude. A finer resolution grid would reduce the plasma bubble placement error.

For simplicity, it should be noted that the inclination angle of the magnetic field line was calculated at an altitude of 200 km instead of the plasma bubble apex height to determine the location of the geomagnetic equator. In order to determine if the approximation was valid, the inclination angle at 200 km was compared to the inclination angle at each plasma bubble apex height. For the largest plasma bubbles of 5000 km base extent, an average inclination angle difference of 0.003 degrees was calculated, indicating that the inclination angle approximation was excellent.

3.2.3 Plasma Bubble Alignment

The plasma bubbles were aligned with Earth's magnetic field as depicted in Figure 10. The WMM function was used to determine the magnetic declination angle (θ) at each geographic latitude, longitude and altitude grid point in the IFM. Starting at an altitude of 200 km at the geomagnetic equator, the magnetic declination was calculated. The change in longitude (ΔLon), measured in degrees, was determined using the equation

$$\Delta Lon = (\Delta Lat) \cdot \tan(\theta_{declination}) \quad (7)$$

where $\theta_{declination}$ is the declination angle and ΔLat is the change in latitude (1.5 degrees). Similar to vector addition, ΔLon was added to ΔLat and rounded to nearest IFM grid point. After determining the magnetic declination angle at the new grid point, ΔLon was calculated, added with ΔLat and rounded to the nearest grid point. This process continued until all plasma bubble grid points at all altitudes were aligned before addressing the next plasma bubble.

The results of the plasma bubble alignment at different altitudes are presented in a series of three panels, labeled (a-c), in Figure 11. With increasing altitude, the north-south extent of the plasma bubbles decreases and becomes more aligned with the geographic longitude. Greater magnetic declinations resulted in larger changes in

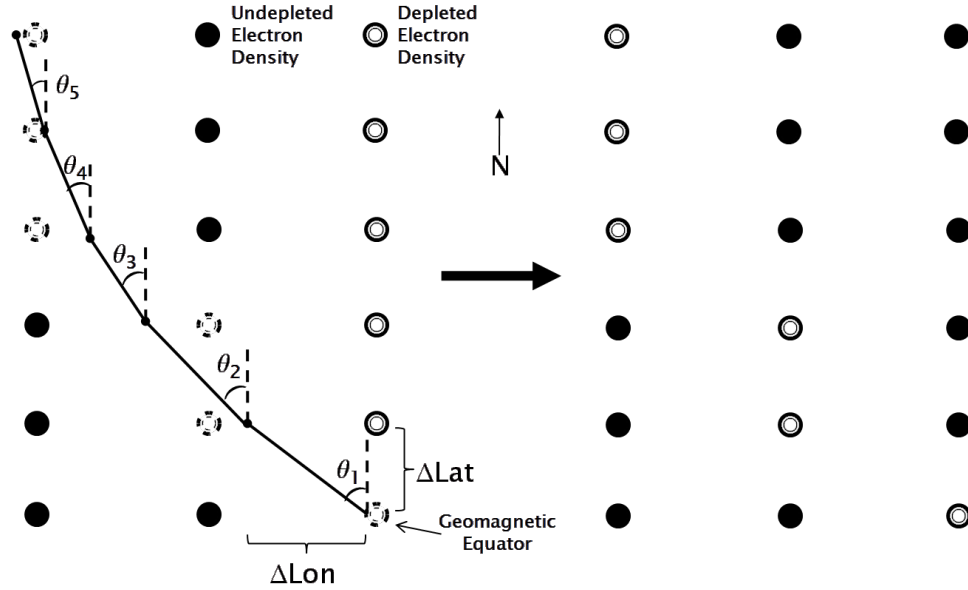
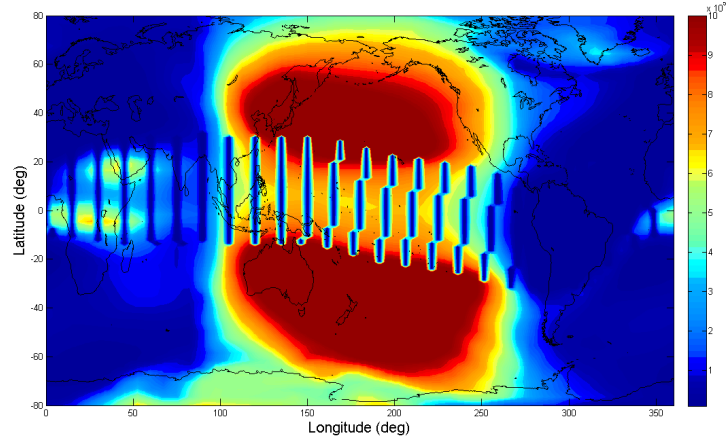


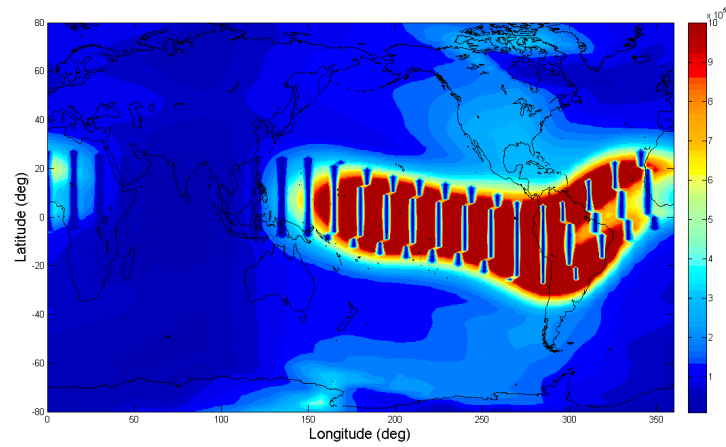
Figure 10. Process of aligning plasma bubbles with Earth's geomagnetic field. The white and black circles represent depleted and undepleted electron densities on a geographic grid, respectively. The dashed circles represent "mapped" plasma bubble grid points. θ represents different magnetic declination angles at each IFM grid point.

longitude. Over Africa and Asia, for example, the plasma bubbles are parallel with lines of geographic longitude. Over the Eastern Pacific, the plasma bubbles have a positive slope relative to the geographic longitude, and over South America and the Atlantic Ocean, a negative slope. Because of the profile of the geomagnetic equator, it is expected that the alignment of the plasma bubbles will result in different affected look angles for different geographic regions.

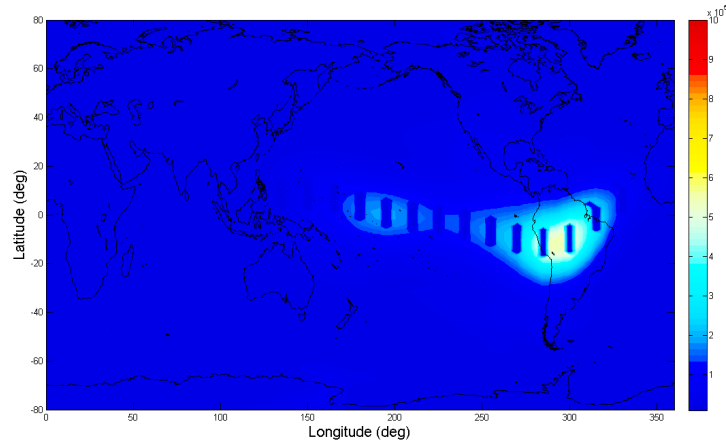
Since the WMM function can only calculate declination angles for altitudes below 1000 km, it was anticipated that there would be consequences when aligning plasma bubbles of 4500 and 5000 km base extent whose apex heights exceed 1000 km. For these plasma bubble sizes, the magnetic declination angle at 1000 km was used at each altitude grid point above 1000 km. In order to determine the validity of this approximation, the declination angles above 1000 km were interpolated at the plasma bubble apex heights of 1054 and 1358 km, respectively, for each analysis region de-



(a) 250 km



(b) 750 km



(c) 1250 km

Figure 11. Altitude slices of plasma bubbles with 5000 km base extent and a factor of 1000 depletion embedded in the IFM at 0000 Universal Time (UT). The plasma bubbles are globally spaced 15 degrees apart in longitude. The increased plasma densities at higher altitudes are due to the Appleton anomaly. The scale on the right side of the figure ranges from 0 to 10×10^5 electrons/cm³.

fined in Figure 6. The declination angle differences between the plasma bubble apex altitudes and the corresponding declination angles at 1000 km were determined. The largest calculated declination angle difference was 1.72 degrees in the Atlantic region for plasma bubbles of 5000 km base extent. Overall, the differences for each analysis region were negligible; using the declination angle approximation was acceptable.

3.3 Development of Utilities

In order to efficiently determine the affected look angles and slant TEC differences, utilities were developed to streamline the calculation process. The utilities that were adapted and developed for the look angle and slant TEC analyses are listed in Table 5. The look angle algorithm was obtained from an azimuth and elevation angle calculator from a satellite communications website and converted into MATLAB code [16]. A copy of the look angle calculation code can be obtained by contacting Satcom Online at comments@satcom.co.uk. The look angle calculation code uses the WGS-84 constants to model the shape of the Earth and trigonometry to calculate the elevation and azimuth angles between any two points identified by geographic latitude, longitude and altitude. The look angle calculation code was incorporated into the look angle analysis and slant TEC algorithms. A five degree elevation mask was used as a conservative estimate in order to mimic realistic GPS ground station practices. Typical elevation masks range between 10 and 15 degrees [12].

The slant TEC calculation code was provided by Utah State University (USU) and converted from the FORTRAN programming language into MATLAB code. A copy of the original slant TEC calculation code can be obtained by contacting the Center for Atmospheric and Space Sciences (CASS) at USU. The slant TEC calculation code determines the TEC between two points identified in Earth-Centered Earth-Fixed (ECEF) coordinates by dividing the slant path into fixed increments and linearly

interpolating the electron densities. Each interpolated electron density is multiplied by the fixed incremental distance to determine the TEC for the slant path segment. The TEC values for each segment are totaled to determine the slant TEC value for the entire slant path.

It was discovered that the slant TEC calculation code directly affects the plasma bubble width. Plasma bubbles placed in the modified 3.75 degree longitude resolution IFM grid resulted in a density depleted region 7.5 degrees in width (about 800 km), the typical width of a plasma bubble. The influence of the interpolation scheme on the plasma bubble width is illustrated in Figure 12. Because of the interpolation scheme, the depletion factor is not constant, but decreases linearly from a maximum at the plasma bubble grid point to a value of zero at the next longitudinal grid point located 3.75 degrees to the east and west, resulting in a total depletion width of 7.5 degrees. In the original 7.5 degree longitude grid, the depletion width would have been 15 degrees in longitude, too wide for a typical bubble. In order to achieve a constant electron density depletion 3.75 degrees longitude in width, two consecutive grid points would have to be depleted. The resulting depletion width would also have been too large at 11.25 degrees, as illustrated in Figure 12. When weighing the two depletion options, depleting only one longitudinal grid point was more representative of the typical plasma bubble width. In addition to the longitudinal direction, the

Table 5. MATLAB Utilities

Adapted	Created	Ensemble
Look angle calculation Slant TEC calculation	Locate geomagnetic equator Determine magnetic declination Increase grid spatial resolution Form plasma bubble shape Align bubbles with magnetic field Deplete IFM electron densities Corotate plasma bubbles Plotting (various)	Look angle analysis Slant TEC analysis

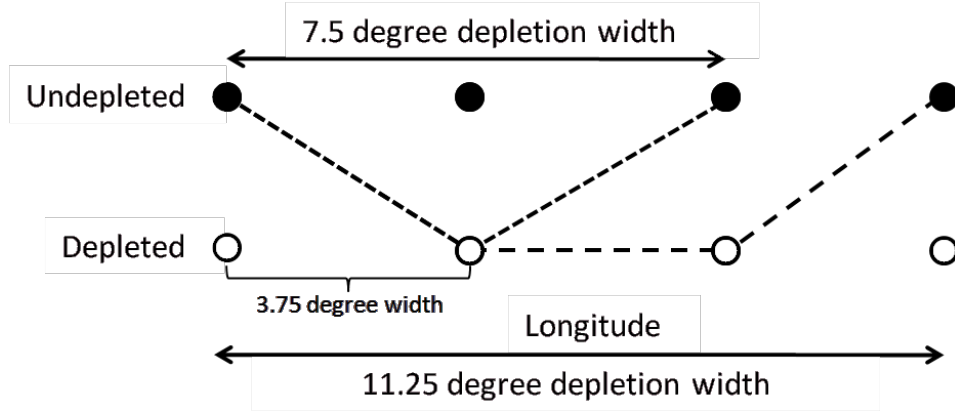


Figure 12. Comparison of depletion widths between plasma bubbles placed along one longitude and two consecutive longitudes.

slant TEC calculation code also modifies the plasma bubble structure in latitude and altitude, elongating the north-south extent of the density depletion region and increasing the apex height.

The ensemble algorithms combine both the adapted and created analysis utilities into an integrated environment, relieving the user from constantly referencing different sources to calculate a particular value. The look angle and slant TEC analysis algorithms are described in further detail in the following sections. The MATLAB code for the created and ensemble algorithms listed in Table 5 is available from the author or from the Department of Engineering Physics at the Air Force Institute of Technology (AFIT).

3.4 Look Angle Analysis

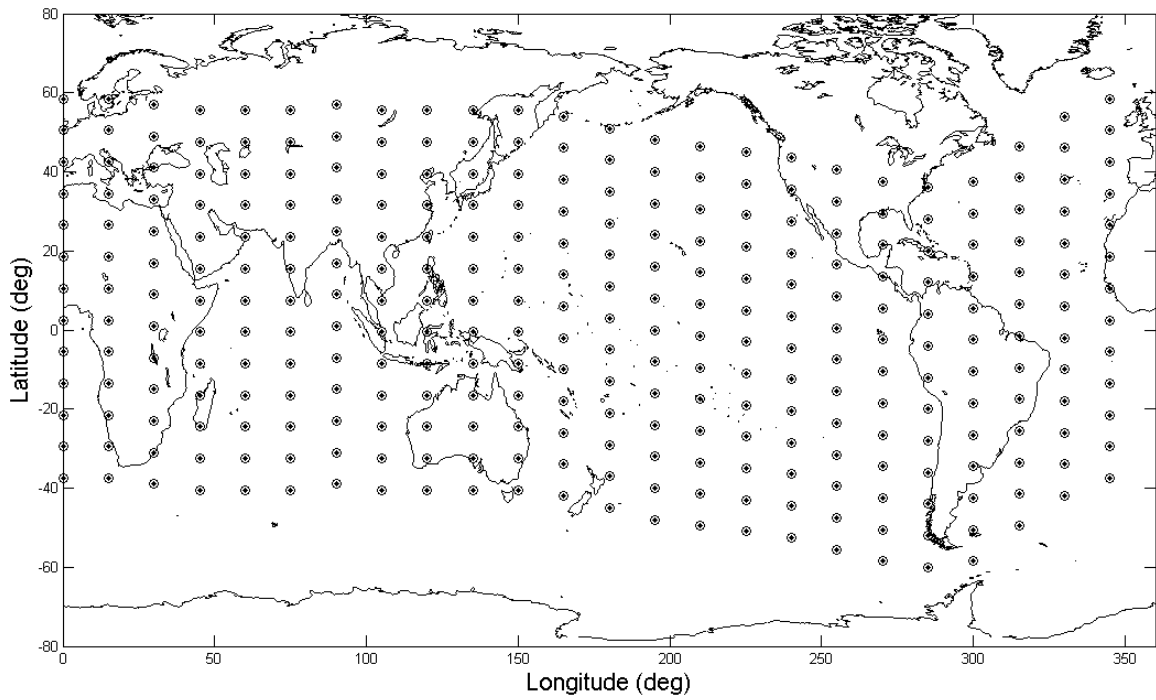
The look angle analysis algorithm identifies slant paths from a GPS ground station that intercept plasma bubble regions. At a selected time, affected azimuth and elevation angles are calculated from GPS ground stations to IFM grid points associated with plasma bubbles placed side-by-side at consecutive longitudes. This method ensures that every possible affected look angle that penetrates a plasma bubble region

is identified.

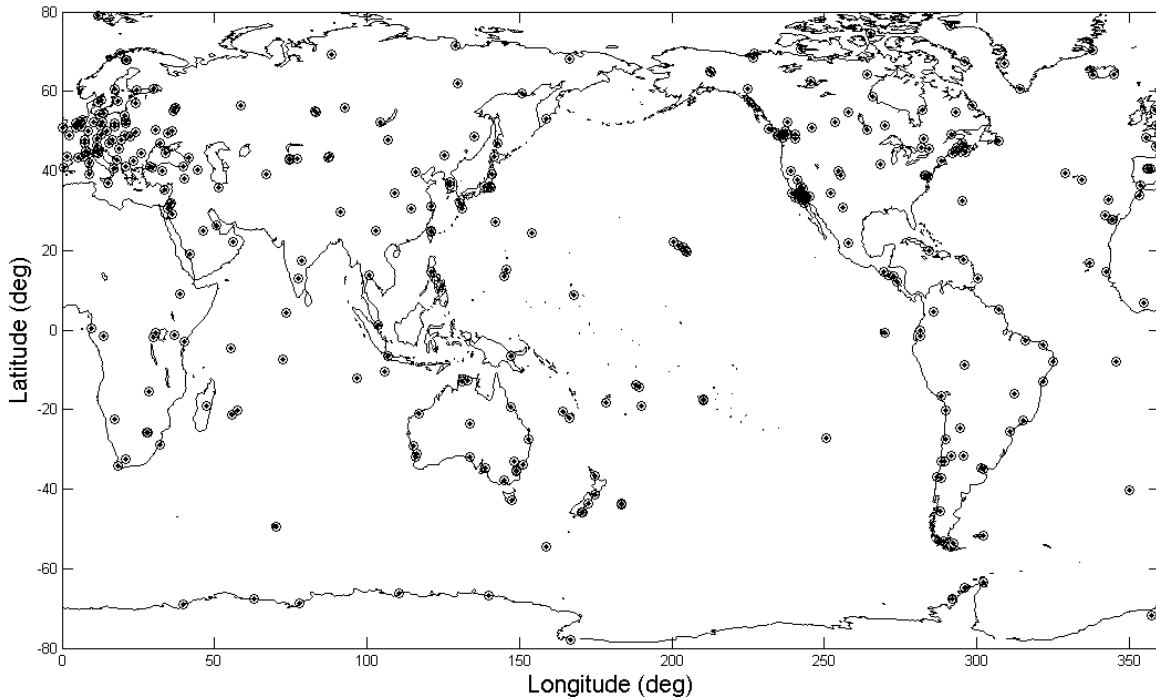
Two different GPS ground station grids were created for the look angle analysis as depicted in Figure 13. First, an evenly spaced grid of 312 ground stations, or IDEAL grid, was created and aligned with the geomagnetic equator as shown in panel (a). The grid points are spaced 15 degrees apart in longitude, 8 degrees in latitude and located at sea level. The IDEAL grid eliminated sparse data regions, especially over the oceans, and facilitated the comparison of affected look angles between GPS ground stations. The second grid, or REAL grid, maps 421 actual GPS ground stations worldwide and is presented in panel (b). The coordinates of the GPS ground stations were obtained from the International GNSS Service (IGS) database [5].

First, plasma bubbles were created and embedded into the IFM electron density grid. Because calculating affected look angles was the purpose of the analysis, the plasma bubbles were placed in an arbitrary IFM electron density map. Simulating quiet geomagnetic conditions, the plasma bubbles were generated instantaneously at 2000 LT and placed at consecutive longitudinal grid points before dissipating at 0515 LT for a total of 37 bubbles. In order to be consistent with the plasma bubble placement in the slant TEC analysis, described in the following section, the most westward plasma bubble was placed at 0500 LT. In addition, the exact time of plasma bubble dissipation in the ionosphere is unknown since ionization can even occur before sunrise at the Earth's surface.

A GPS ground station in the IDEAL or REAL grid was then selected and the azimuth and elevation angles from the ground station to each plasma bubble grid point were calculated. Only look angles whose elevation angles were greater than the five degree elevation mask were recorded. Next, another GPS ground station was selected and the process repeated. After all GPS ground stations were analyzed, a new



(a) IDEAL Grid



(b) REAL Grid

Figure 13. GPS ground station grids: (a) IDEAL grid, b)REAL grid.

plasma bubble formed to the west and the most eastward bubble dissipated, shifting the entire plasma bubble region 3.75 degrees in longitude to the west over a period of 15 minutes. Affected look angles for all GPS ground stations were calculated again in the same manner. After a 24 hour period, the plasma bubble size was increased and the entire process was repeated again. Once all plasma bubble sizes were analyzed, the algorithm terminated. A flow diagram of the look angle analysis is presented in Figure 14.

3.5 Slant TEC Analysis

The slant TEC analysis is similar to the look angle analysis, but incorporates GPS satellite positions. Instead of calculating affected look angles between GPS ground stations and plasma bubble grid points, the slant TEC analysis calculates affected look angles and the corresponding slant TEC between each GPS ground station and a standard set of GPS satellite positions presented in Figure 15. The GPS satellite position data was obtained from the Crustal Dynamics Data Information System (CDDIS) GNSS website in the form of a .sp3 (Standard Product #3) file [11]. The .sp3 orbit positions are considered the international standard and are used when there is need for precision [3]. The slant TEC analysis investigates the 27 different geophysical conditions listed in Table 3 and the 15 different bubble configurations in Table 4. Both the IDEAL and REAL grids were also used.

A flow diagram of the slant TEC analysis is depicted in Figure 16. First, a geophysical condition was selected. For quiet geomagnetic conditions ($K_p = 1$), plasma bubbles were generated from 2000 LT to 0600 LT, spaced one hour apart (15 degrees longitude) and embedded into the IFM electron density grid. For active geomagnetic conditions ($K_p \geq 5$), plasma bubbles started at 0000 LT (midnight) and were placed one hour apart until 0600 LT. Next, a GPS ground station in the REAL or IDEAL

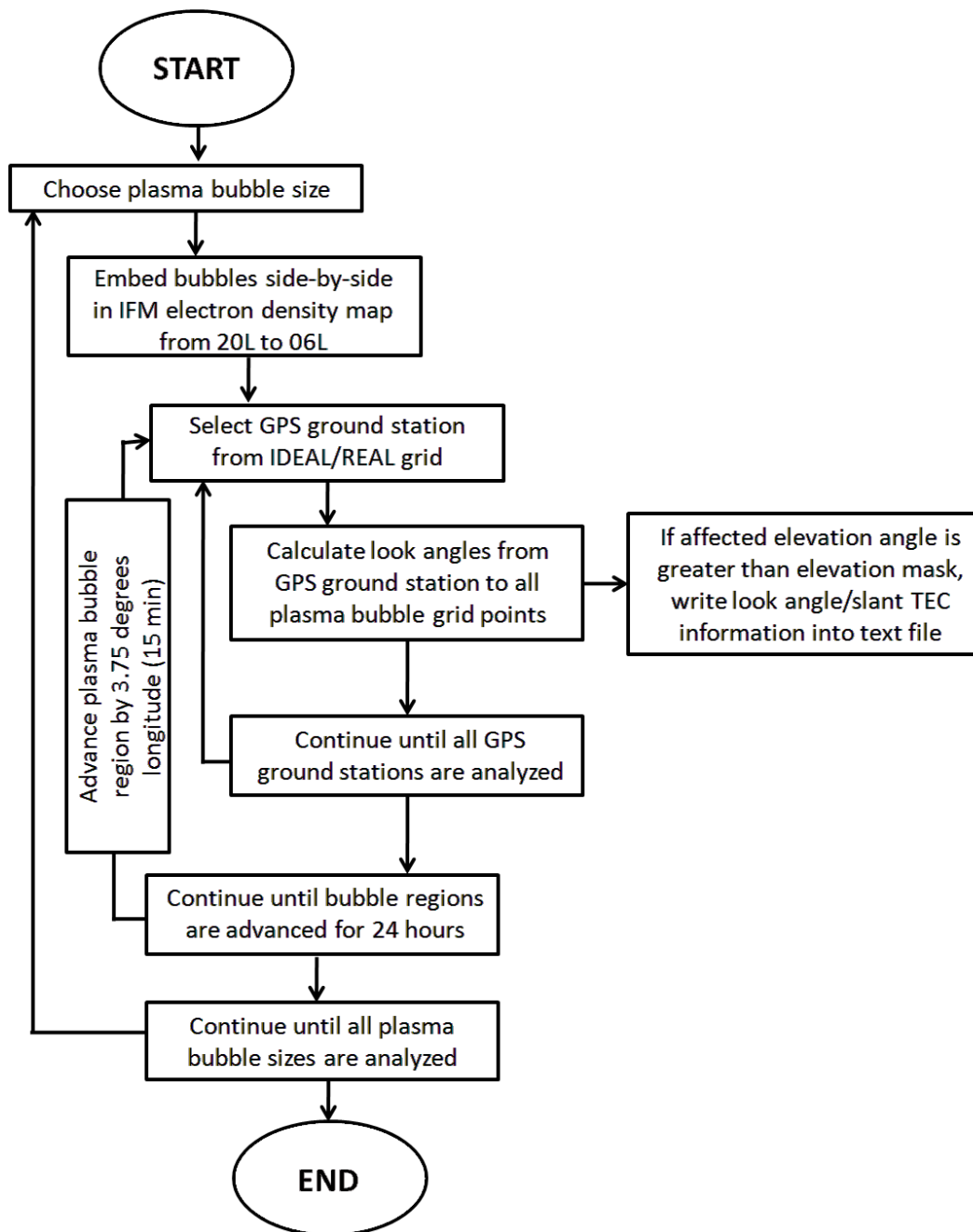


Figure 14. Flow diagram of the look angle analysis algorithm.

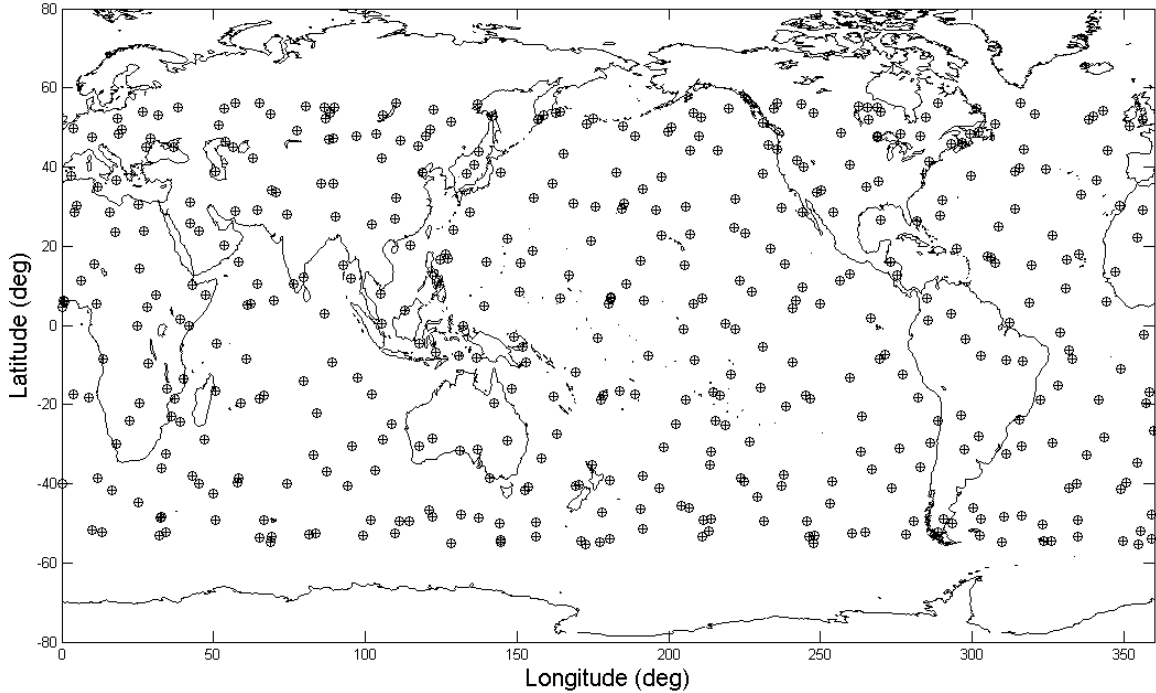


Figure 15. Standard set of GPS satellite positions over a 24 hour period.

GPS ground station grid was selected and the affected look angles and slant TEC to each GPS satellite position were calculated. If the calculated elevation angle was greater than the 5 degree elevation mask, the look angle and slant TEC data were recorded. The slant TEC calculations were conducted using the IFM electron density map with and without embedded plasma bubbles, enabling differences in slant TEC to be characterized.

Next, another GPS ground station was selected and the process was repeated. After all GPS ground stations were analyzed, the IFM electron density map was advanced by one hour causing a new plasma bubble to form 15 degrees to the west and the most eastward bubble at 0600 LT to dissipate. Affected look angles and slant TEC values were again calculated in the same manner for all GPS ground stations. After a 24 hour period, another plasma bubble configuration was selected and the process was repeated for all GPS ground stations. After all plasma bubble

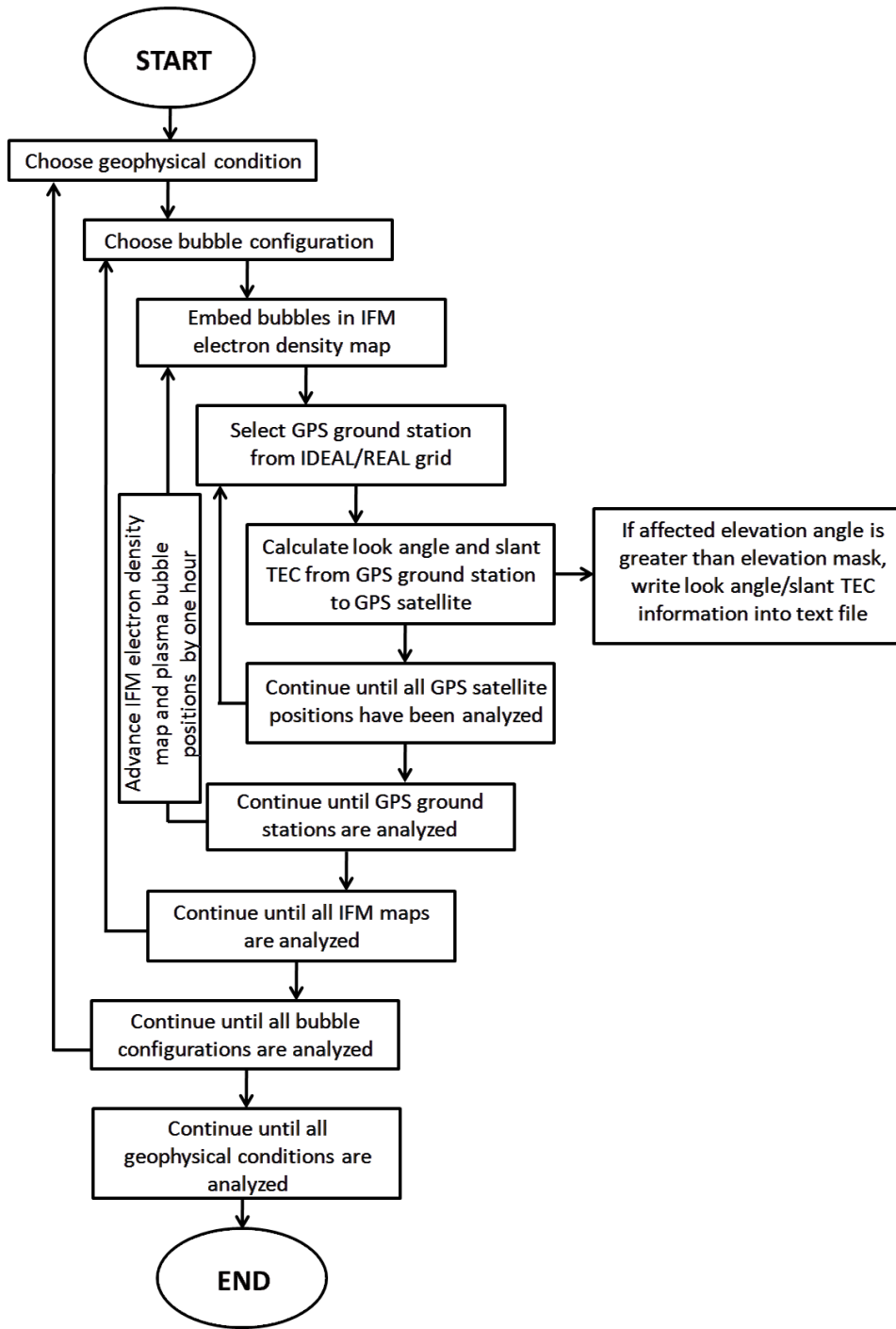


Figure 16. Flow diagram of the slant TEC analysis algorithm.

configurations were addressed, another geophysical condition was selected and after all 27 geophysical conditions were analyzed, the algorithm terminated.

3.6 Plasma Bubble Occurrence Statistics

In order to exploit the look angle and slant TEC results for all 27 geophysical conditions, Figure 6 was referenced to indicate the probability of plasma bubble formation according to year (solar activity), month (season) and geographic region (longitude). Dividing the IDEAL grid into five analysis regions to match the geographic areas defined in the plasma bubble occurrence statistics enabled a regional characterization of the results to be conducted. For easier comparison, an arbitrary longitude of 13 GPS ground stations was chosen in each analysis region to represent the typical regional results. The five analysis regions are defined in Table 6 and illustrated in Figure 17. The next chapter will present and analyze the results of the look angle and slant TEC analyses.

Table 6. Analysis Regions

Region	Longitude Range	Analysis Longitude
African	340E - 060E	030E
Asian	060E - 160E	105E
Central Pacific	160E - 240E	195E
Western Pacific	240E - 300E	270E
Atlantic	300E - 340E	315E

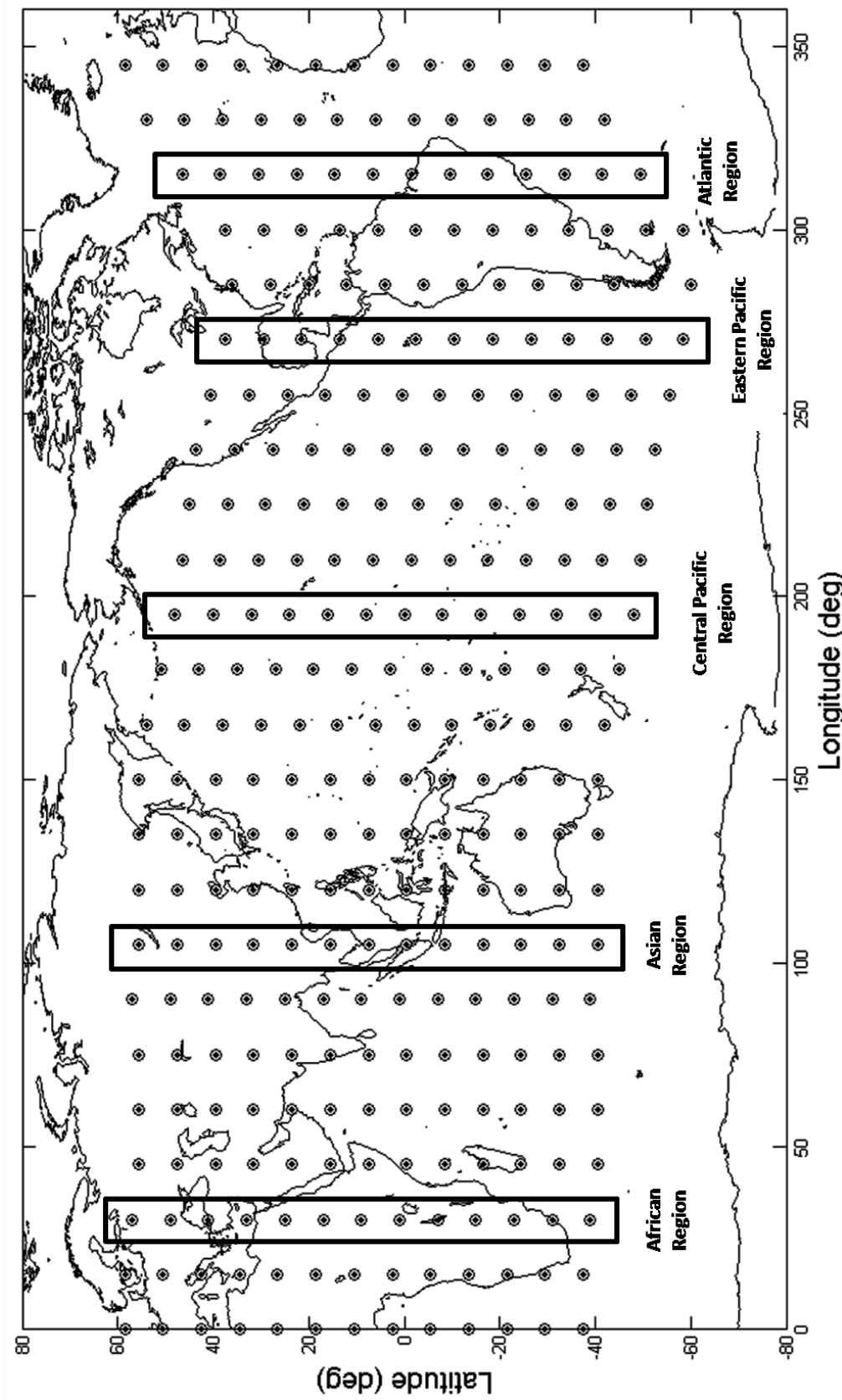


Figure 17. Regional longitudes used to compare the results of the look angle and slant TEC analyses.

IV. Results and Analysis

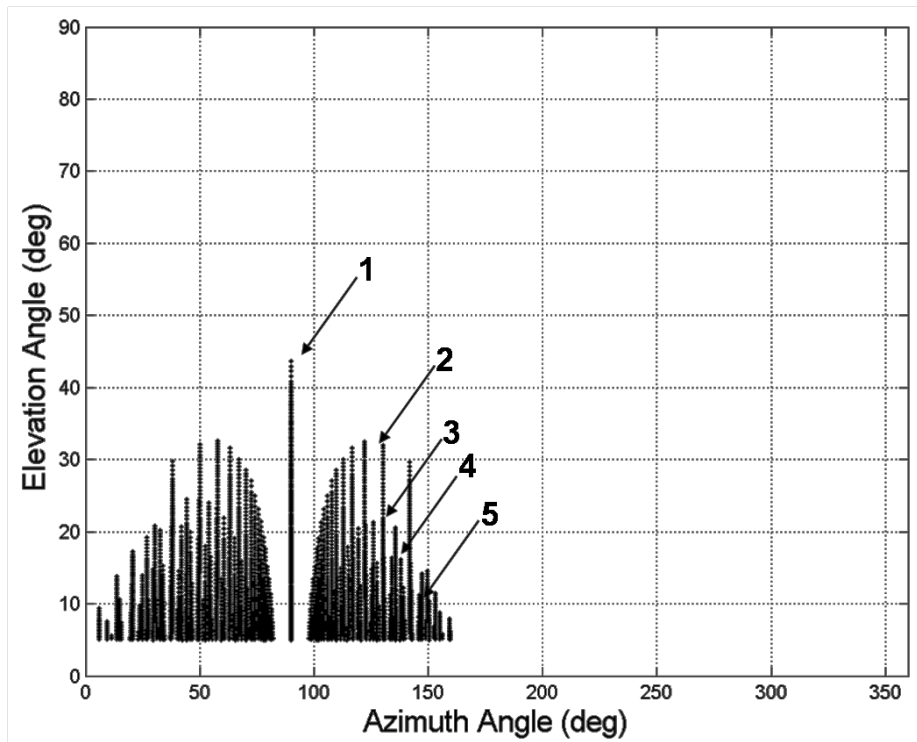
This chapter will present and analyze the results of the look angle and slant TEC analyses. The results of the look angle analysis will be used to compare affected look angle profiles for different plasma bubble configurations and different geographic locations. The results will also be used to determine how the generation and dissipation of plasma bubbles change affected look angles over time. Afterwards, the results of the slant TEC analysis will be used to determine how plasma bubbles affect slant TEC measurements for different plasma bubble configurations and geophysical conditions.

4.1 Look Angle Analysis

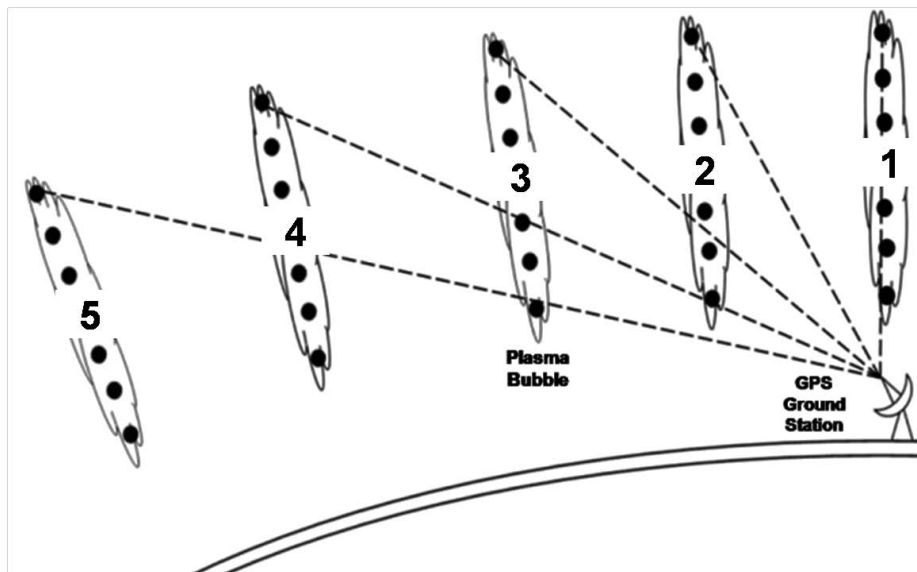
The results of the look angle analysis will be presented in two parts. First, the affected look angles will be analyzed according to plasma bubble size, distance from the geomagnetic equator and geographic region. Next, the evolution of affected azimuth and elevation angles over time will be presented. Even though the look angle analysis was conducted using both IDEAL and REAL grids, only the IDEAL grid results will be presented for easier comparison.

4.1.1 Look Angle Profiles

An example of an affected look angle profile is shown in panel (a) of Figure 18 at a GPS ground station located 24 degrees latitude south of the geomagnetic equator at 0000 LT. Each data point represents a corresponding elevation and azimuth angle affected by the presence of plasma bubbles. An azimuth angle of 0 degrees looks toward the east and an azimuth angle of 90 degrees points to the north. The gaps between data points are due to the coarse IFM grid resolution in latitude, longitude and altitude. The arrows identify plasma bubbles that can be seen from the GPS



(a) Affected Look Angle Profile



(b) Affected Look Angle Depiction

Figure 18. Affected look angle profiles at 0000 LT plotted in Cartesian and polar coordinates for a GPS ground station located 24 degrees latitude south of the geomagnetic equator in the African region for plasma bubbles of 5000 km base extent. An azimuth angle of 0 degrees is east and 90 degrees is north. Arrows in panel (a) correspond with the plasma bubbles numbered in the affected look angle depiction in panel (b).

ground station and correspond with the bubbles in the look angle depiction in panel (b). The elevation maximum at 90 degrees (north) is the result of viewing plasma bubble 1 along its north-south extent. Plasma bubble 2 and subsequent plasma bubbles are located in 3.75 degree longitude increments to the west. Because of the curvature of the Earth, only portions of plasma bubbles at farther distances are detected, resulting in lower affected elevation angles. Overall, the upside-down watermelon shape of the plasma bubbles elongated along the dipolar field lines is evident.

4.1.1.1 Bubble Size Comparison

A comparison of affected look angle profiles for different plasma bubble sizes is presented in Figure 19 at a GPS ground station located 16 degrees latitude south of the geomagnetic equator in the African region at 0000 LT. The figure consists of five panels, labeled (a-e), which correspond with plasma bubble base extents from 3000 to 5000 km. The smaller bubbles in panels (a-c) resulted in a smaller range of affected elevation and azimuth angles compared to the larger bubbles in panels (d) and (e). For this particular GPS ground station, the figure shows that plasma bubbles with a base extent greater than 4000 km, panels (c-d), extended over the GPS ground station, affecting azimuth angles to the south. Elevation maximums, located at azimuth angles of 90 and 270 degrees, are a result of viewing a plasma bubble along its north and south extent, respectively. The breaks in the affected elevation angles are due to the spacing between IFM altitude grid points.

4.1.1.2 Latitude Comparison

In the same format as Figure 19, a graphics array of affected look angle profiles is presented in Figure 20 in order to compare affected look angles at different distances

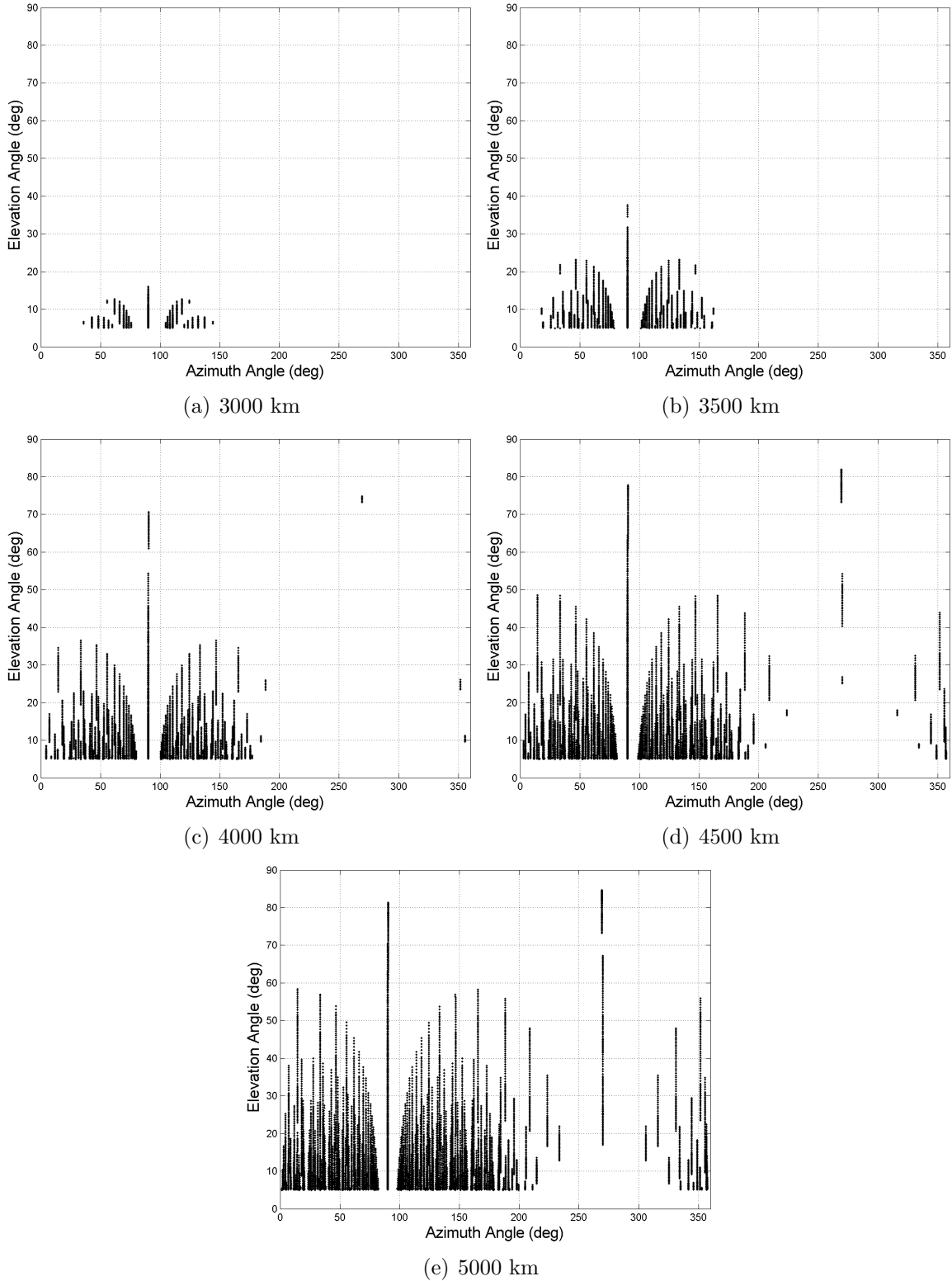


Figure 19. Affected look angles at 0000 LT for the five different plasma bubble sizes at a GPS ground station located 16 degrees latitude south of the geomagnetic equator in the African region.

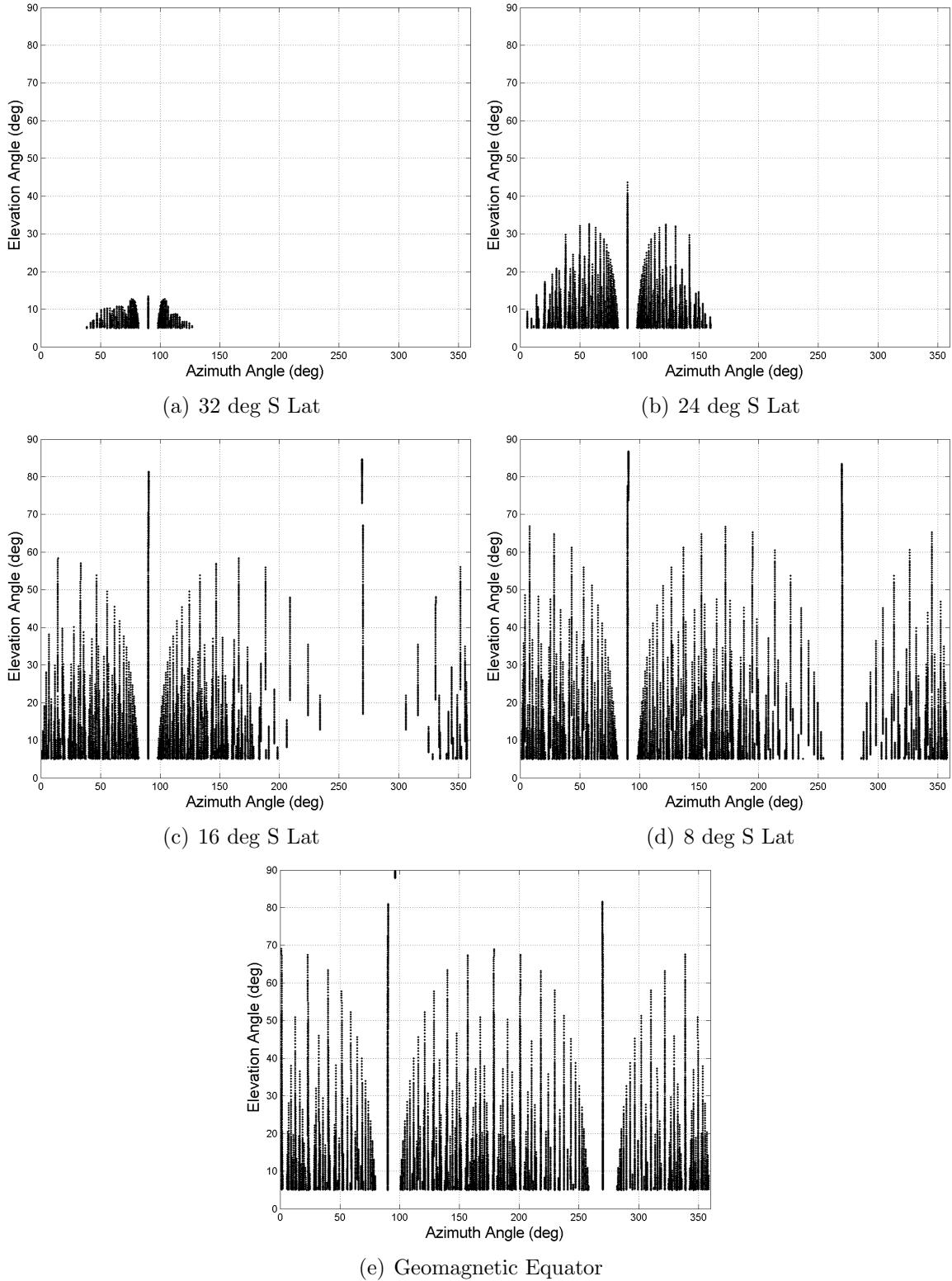


Figure 20. Affected look angle profiles at 0000 LT for GPS ground stations in the African region at different distances from the geomagnetic equator using plasma bubbles of 5000 km base extent.

from the geomagnetic equator. Each of the five panels, labeled (a-e), shows affected look angles for different GPS ground stations spaced eight degrees apart in latitude from the geomagnetic equator in the African region for plasma bubbles of 5000 km base extent. The figure indicates that the range of affected elevation and azimuth angles is dependent on distance from the geomagnetic equator. Panels (a) through (d) show increasing affected azimuth and elevation angles for GPS ground stations located closer the geomagnetic equator.

At the geomagnetic equator, panel (e), the maximum azimuth and elevation angles are affected because a greater number of plasma bubbles can be seen. The affected look angles at an azimuth angle of 95 degrees and an elevation angle of 90 degrees are the result of the look angle calculation algorithm. In reality, these look angles are located directly overhead of the GPS ground station. The vertical elevation angles cause the look angle algorithm to miscalculate the corresponding affected azimuth angles. The vertical look angle miscalculation only occurs at GPS ground stations located at the geomagnetic equator.

By examining the affected look angle profiles at two GPS ground stations located at equal distances from the geomagnetic equator, an asymmetry is observed. Two GPS ground stations located 32 degrees south and north of the geomagnetic equator are presented in panels (a) and (b) of Figure 21. The figure shows that the maximum affected elevation angle at the northern station in panel (b) is greater. This asymmetry can be explained by the illustration in Figure 22. The Earth is not a perfect sphere, but an oblate spheroid with a bulge at the geographic equator. Because of the equatorial bulge, the field-of-view of northern GPS ground station is not as limited compared to the southern station. Therefore, the northern GPS ground station is affected by higher elevation angles and a wider range of affected azimuth angles, resulting in asymmetrical affected look angle profiles.

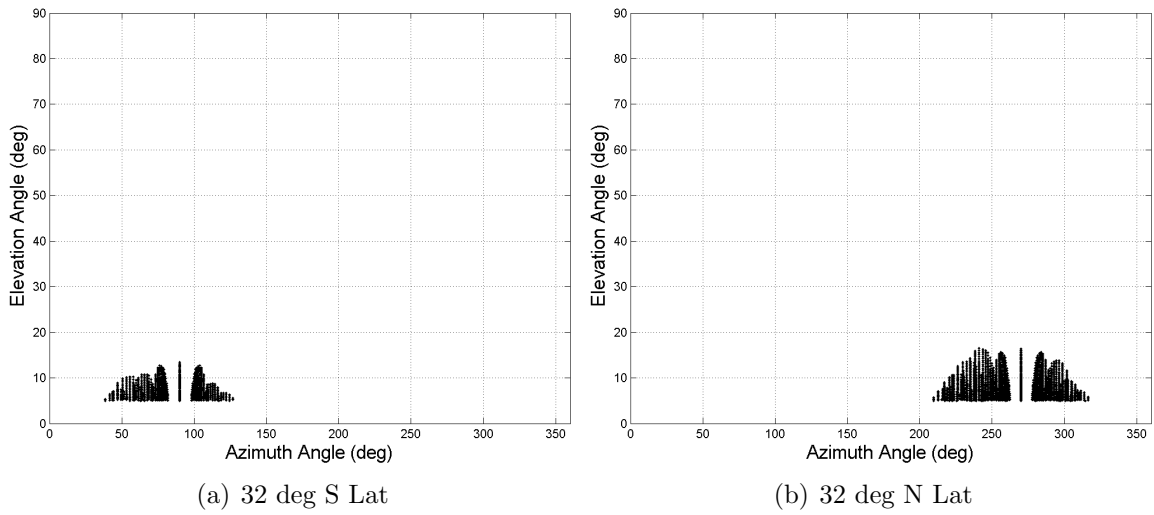


Figure 21. Asymmetrical affected look angle profiles at 0000 LT for GPS ground stations in the African region at equal distances from the geomagnetic equator using plasma bubbles of 5000 km base extent.

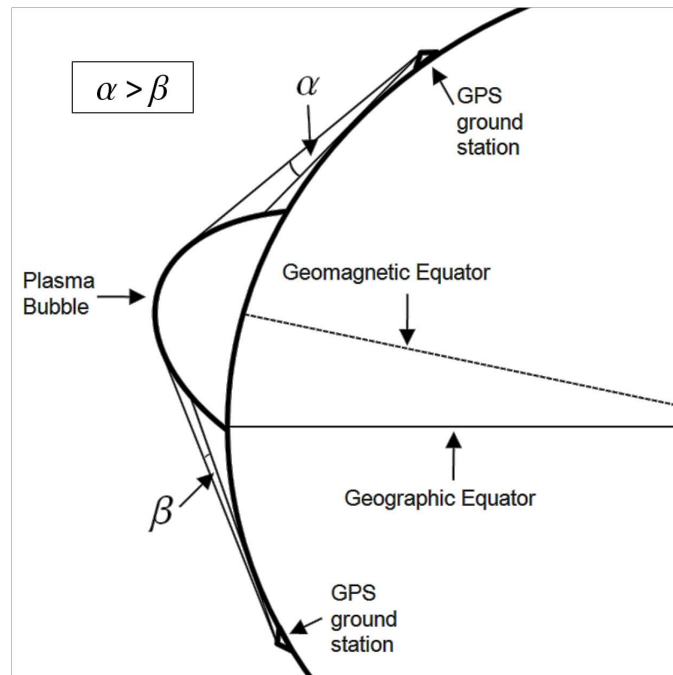


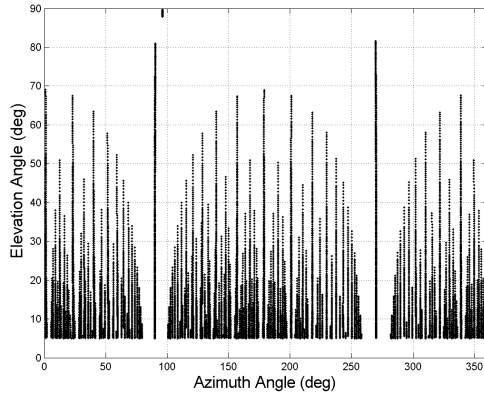
Figure 22. Look angle asymmetry depiction. See text.

4.1.1.3 Regional Comparison

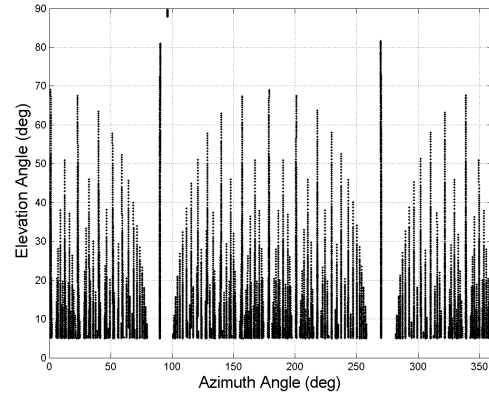
For GPS ground stations located at the geomagnetic equator, affected look angle profiles are compared in Figure 23 for different analysis regions using plasma bubbles of 5000 km base extent. The figure consists of five panels, labeled (a-e), that correspond with the African, Asian, Central Pacific, Eastern Pacific and Atlantic regions, respectively. The figure indicates that each of the five panels shows slightly different affected look angle profiles as a result of the shape of the geomagnetic equator in each analysis region. In addition, because the GPS ground stations are located at the geomagnetic equator, vertical look angle miscalculations, explained in the previous section, are evident in each panel. At farther distances from the geomagnetic equator, the affected look angle profile differences are more distinguishable for each region since the GPS ground stations are not completely surrounded by plasma bubbles. The affected look angle profiles for GPS ground stations located 32 degrees latitude north of the geomagnetic equator in each analysis region using plasma bubbles of 5000 km base extent are shown in Figure 24, with panels (a) through (e) corresponding to the same analysis regions previously mentioned.

4.1.2 Time Evolution

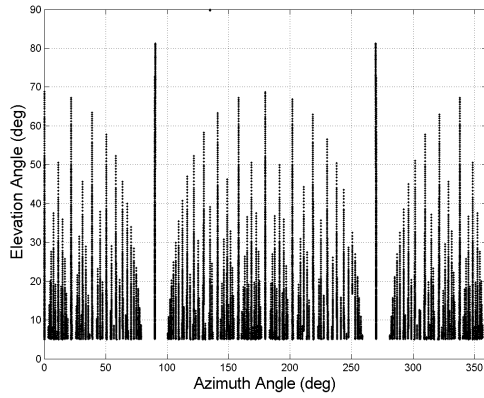
In order to determine how affected azimuth and elevation angles change as plasma bubbles form, corotate and dissipate, the affected look angle profiles at each GPS ground station were analyzed over time. Affected azimuth and elevation angles at a GPS ground station on the geomagnetic equator in the African region for bubbles of 5000 km base extent are presented at different times in Figure 25. The six panels, labeled (a-f), correspond with local times from sunset to sunrise. As a note, the local times in the figure were calculated during equinox and will have to be adjusted accordingly depending on the season.



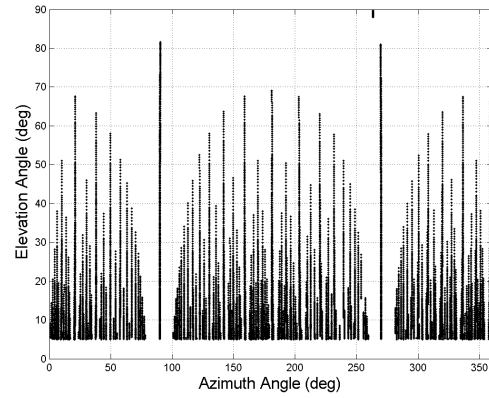
(a) African Region



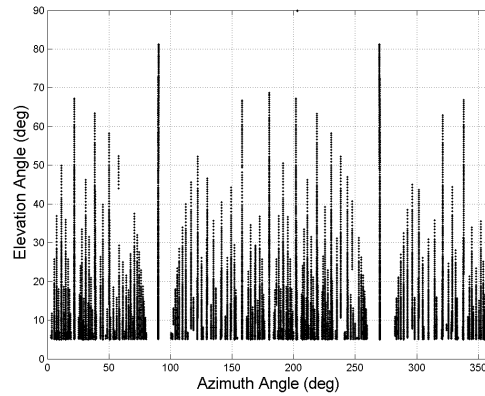
(b) Asian Region



(c) Central Pacific Region

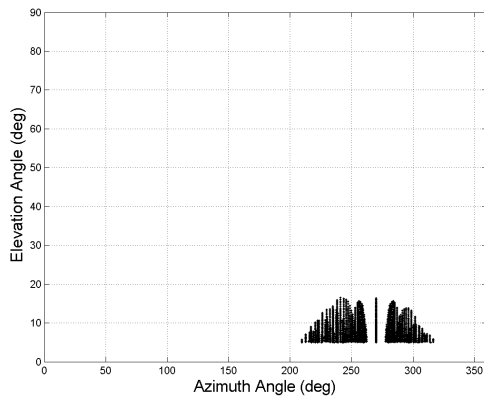


(d) Eastern Pacific Region

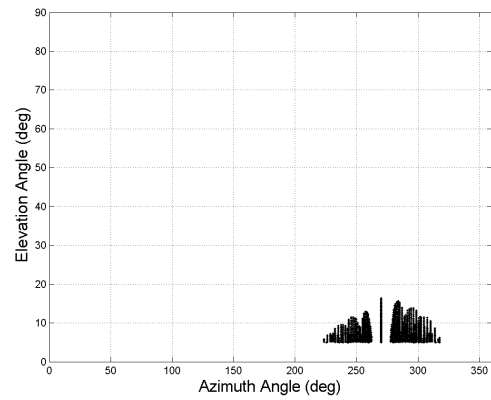


(e) Atlantic Region

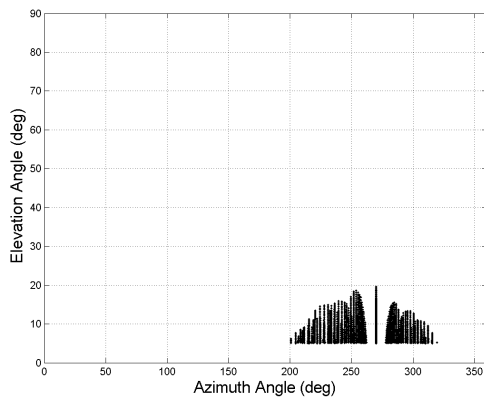
Figure 23. Affected look angle profiles at 0000 LT for plasma bubbles of 5000 km base extent for GPS ground stations located at the geomagnetic equator in each analysis region.



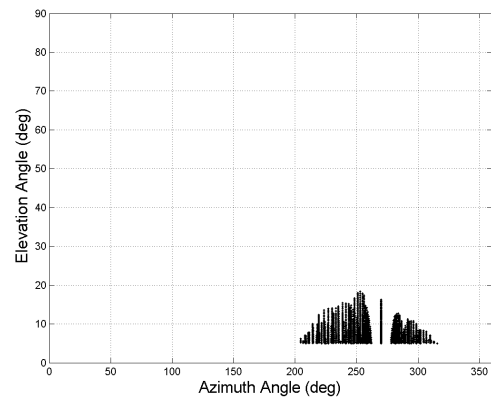
(a) African Region



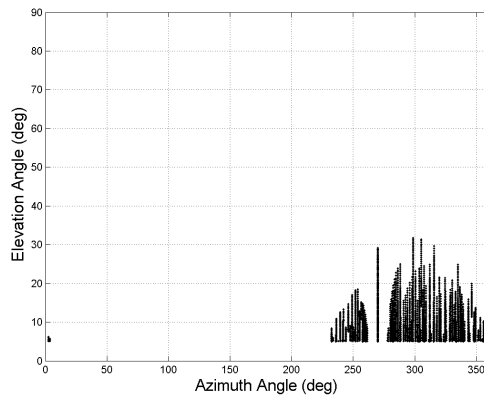
(b) Asian Region



(c) Central Pacific Region



(d) Eastern Pacific Region

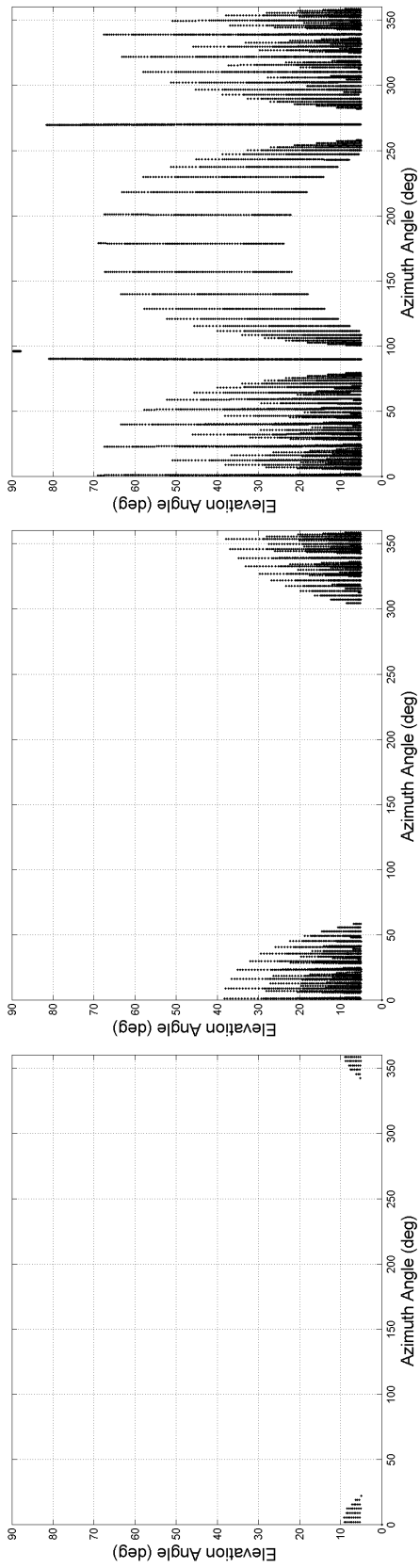


(e) Atlantic Region

Figure 24. Affected look angle profiles at 0000 LT for plasma bubbles of 5000 km base extent for GPS ground stations located 32 degrees latitude north of the geomagnetic equator in each analysis region.

The time series of affected look angle profiles clearly depicts the formation and dissipation of plasma bubbles. At 1830 LT, panel (a) shows affected look angles to the east at low elevations, indicating that plasma bubbles can affect GPS ground stations even before local sunset. Over time, plasma bubbles continue to form westward towards the GPS ground station, presented in panels (b) and (c), increasing the affected elevation and azimuth angles. A plasma bubble located 3.75 degrees to the west of the GPS ground station is shown in panel (c). Because the plasma bubble base starts at an altitude of 200 km, there is an area of unaffected look angles at elevation angles below the plasma bubble base. In the morning hours, panel (g) shows that the affected look angles to the east became unaffected first as plasma bubbles dissipate due to sunrise. As plasma bubbles continue to disappear and fill in over time, the range of affected elevation and azimuth angles decreases as indicated in panels (h) and (i). Overall, the figures illustrate that the greatest changes to the affected look angle profiles occur at sunset and sunrise as plasma bubbles form and dissipate, respectively.

Next, the affected azimuth and elevation angles were analyzed individually to determine how they evolve over time. First, the affected azimuth angles as a function of local time for plasma bubbles of 5000 km base extent at the same GPS ground station are presented in panel (a) of Figure 26. Similar to the results in Figure 25, the figure indicates that azimuth angles to the east are first affected near sunset as plasma bubbles begin to form westward towards the GPS ground station. Furthermore, as the plasma bubbles begin to dissipate in the morning hours, the azimuth angles to the east become unaffected first as the bubbles dissipate toward the west. Applying the results of the bubble configuration analysis in Section 4.1.1.1, it is anticipated that larger plasma bubbles will affect GPS ground stations sooner during the post-sunset formation and for a longer duration during dissipation in the early morning compared



(c) 2030 LT

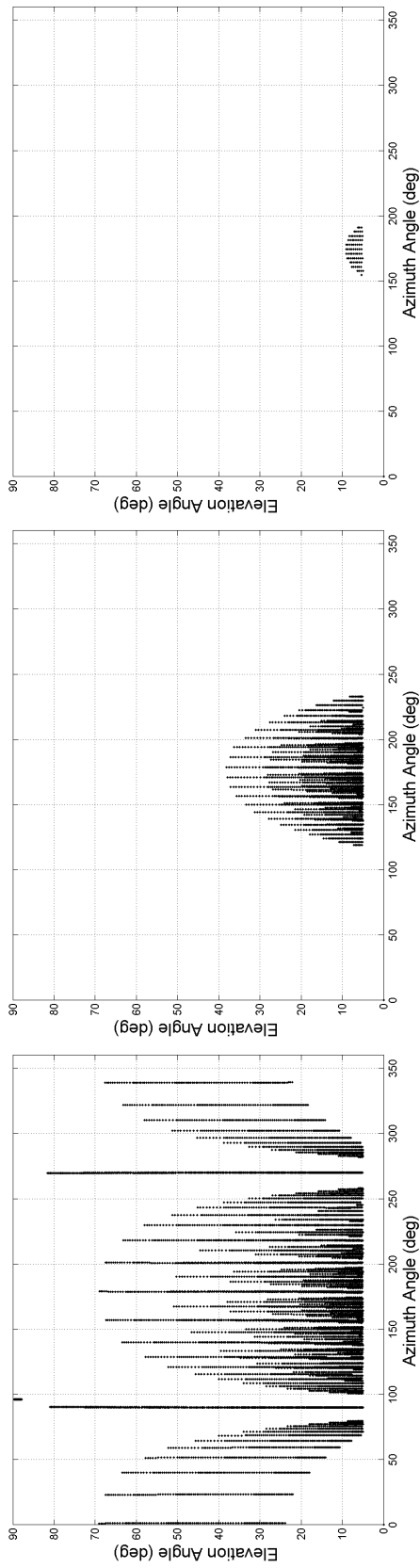


Figure 25. Affected look angle profiles over time for a GPS ground station located on the geomagnetic equator in the African region for bubbles of 5000 km base extent.

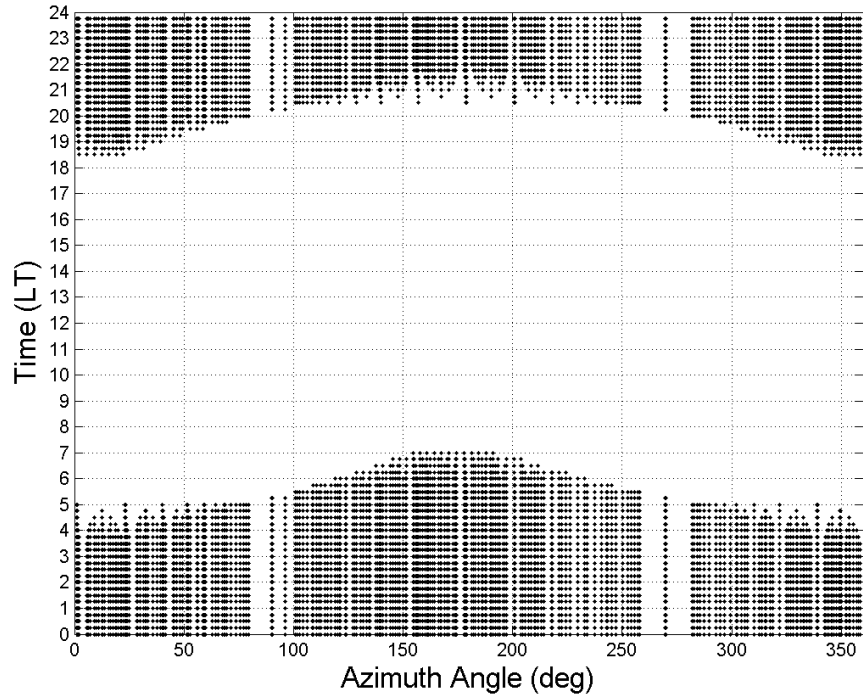
to smaller bubbles.

The affected elevation angles as a function of local time at the same GPS ground station are depicted in panel (b) of Figure 26. As expected, the figure shows that during plasma bubble formation, low elevation angles are affected first as plasma bubbles form to the east. As the plasma bubbles progressively approach the GPS ground station post-sunset, the affected elevation angles increase. After 2015 LT, the figure indicates that the plasma bubbles are located above the GPS ground station resulting in affected elevation angles of 90 degrees. The gap in the data at high elevation angles is a result of the spacing between altitude grid points. In the morning hours, the affected elevation angles decrease as plasma bubbles begin to dissipate. Again, applying the bubble configuration results, it is expected that larger plasma bubbles will also affect GPS ground stations sooner during post-sunset and for a longer duration in the early morning compared to smaller bubbles.

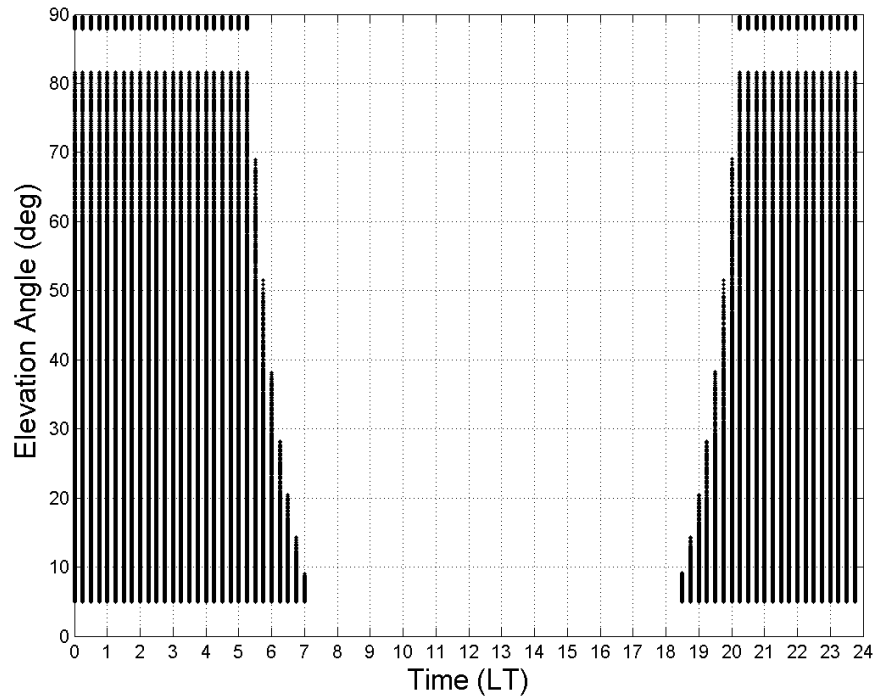
4.2 Slant Total Electron Content Analysis

After analyzing the affected look angle profiles according to plasma bubble size, geographic location and time, the slant TEC analysis will quantify slant TEC differences that can cause significant radio and satellite communication problems. The results of the slant TEC analysis will also be presented in several parts. First, slant TEC differences due to different plasma bubble configurations, listed in Table 7, will be compared. As previously noted, the table lists five different plasma bubble sizes and three different depletion factors to form a total of 15 different plasma bubble configurations. Afterwards, slant TEC differences will be compared according to season, level of solar activity and level of geomagnetic activity.

Before presenting the analysis results, one quantity needs to be defined: slant



(a) Affected Azimuth Angle vs. Time



(b) Affected Elevation Angle vs. Time

Figure 26. (a) Affected azimuth angles and (b) elevations angles as a function of local time for plasma bubbles of 5000 km base extent at a GPS ground station located at the geomagnetic equator in the African region.

Table 7. Slant TEC Analysis Bubble Configurations

Configuration Number	Base Extent	Depletion Factor
1	3000 km	10
2	3000 km	100
3	3000 km	1000
4	3500 km	10
5	3500 km	100
6	3500 km	1000
7	4000 km	10
8	4000 km	100
9	4000 km	1000
10	4500 km	10
11	4500 km	100
12	4500 km	1000
13	5000 km	10
14	5000 km	100
15	5000 km	1000

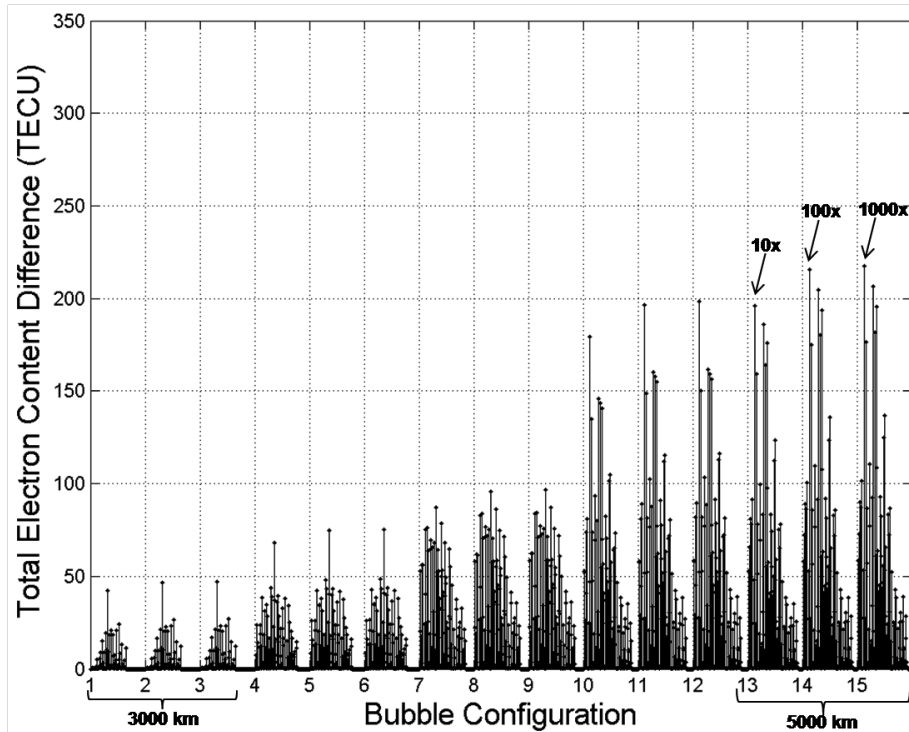
TEC difference. Slant TEC difference (ΔTEC) is defined by the equation

$$\Delta\text{TEC} = \text{TEC}_{\text{without bubbles}} - \text{TEC}_{\text{with bubbles}}. \quad (8)$$

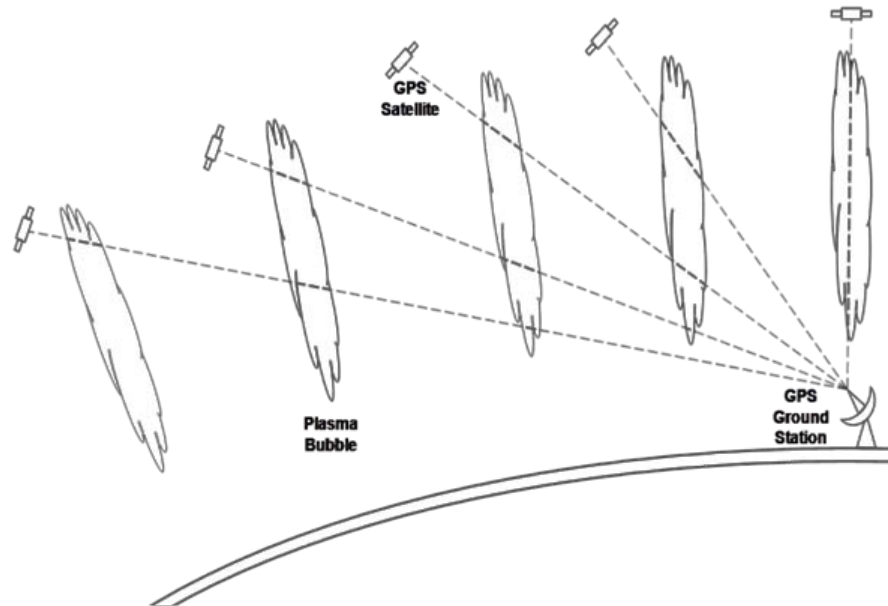
Because plasma bubbles are regions of depleted electron density, the calculated slant TEC value without bubbles will always be greater than the slant TEC value with bubbles. As a result, the slant TEC difference will always be a positive quantity. A slant TEC difference of zero indicates that the slant path intercepted no plasma bubbles.

4.2.1 Bubble Configuration Comparison

Slant TEC differences for different plasma bubble configurations are compared in panel (a) of Figure 27 during equinox, solar maximum and quiet geomagnetic conditions. The GPS ground station is located 8 degrees south of the geomagnetic equator in the Asian region. Each data point corresponds with one slant path between



(a) Slant TEC Difference



(b) Slant TEC Depiction

Figure 27. (a) Slant TEC difference for different plasma bubble configurations at a GPS ground station located 8 degrees south of the geomagnetic equator in the Asian region at equinox (Day 267) during solar maximum ($F_{10.7} = 225$) and quiet geomagnetic conditions ($K_p = 1$). (b) A depiction of slant paths between a GPS ground station and GPS satellites in the presence of plasma bubbles.

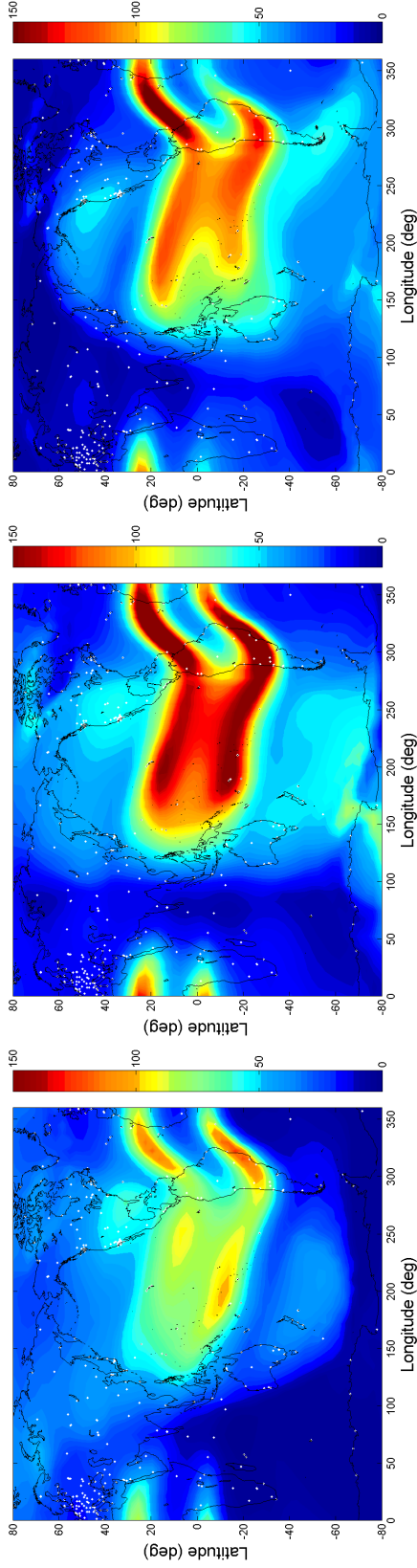
the GPS ground station and a GPS satellite at some point in time.

The figure indicates that slant TEC differences increase with larger plasma bubbles and greater depletion factors. The schematic in panel (b) shows a GPS ground station receiving radio signals from three different GPS satellites. Depending on the look angle to each GPS satellite, each slant path will intercept a different number of plasma bubbles, affecting the calculated slant TEC value. Moreover, larger plasma bubble sizes and greater depletion factors will affect the calculated slant TEC value and, hence, slant TEC difference as indicated in panel (a).

4.2.2 Season

An analysis of slant TEC differences for different seasons is presented in Figure 28. Before presenting the slant TEC results as a function of season, it is helpful to show the seasonal influence on electron density. Vertical TEC values over the different seasons during solar maximum and quiet geomagnetic conditions are presented in panels (a-c) of Figure 28 as a function of latitude and longitude, corresponding with the seasons of summer, equinox and winter, respectively. During the summer and winter seasons, shown in panels (a) and (c), the largest electron densities are more concentrated to the south and north of the geomagnetic equator, respectively, as thermospheric winds shift the electron density concentrations away from the geomagnetic equator. During equinox, shown in panel (b), the thermospheric winds concentrate the electron densities near the geomagnetic equator where the plasma bubbles form.

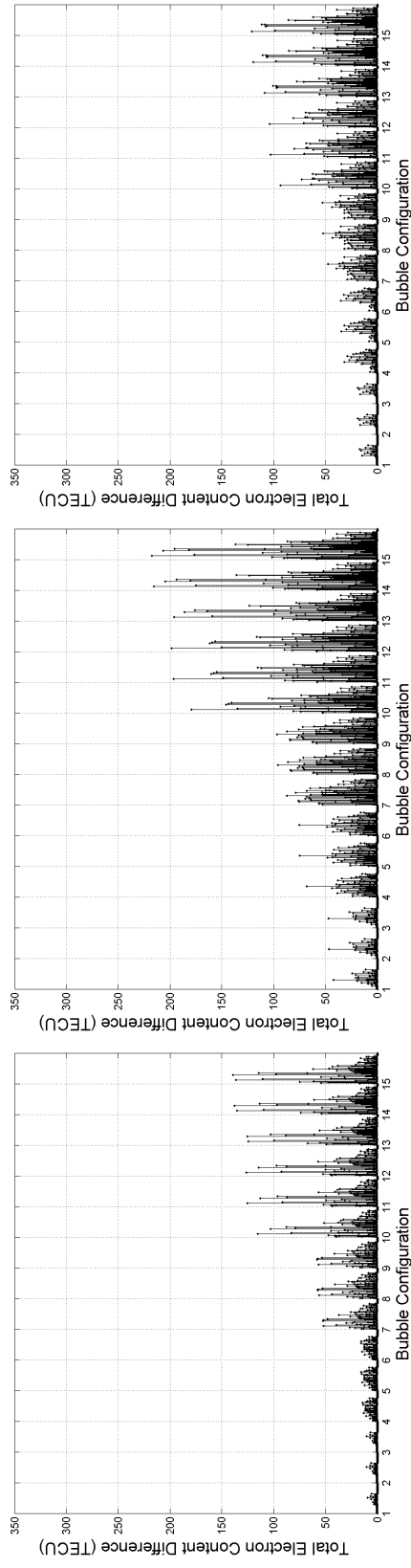
Slant TEC differences as a function of season for different bubble configurations at a GPS ground station located at the geomagnetic equator during solar maximum and quiet geomagnetic conditions are shown in panels (d-f) of Figure 28. The figure indicates that slant TEC differences are greatest during equinox, shown in panel (e), compared to summer and winter. Because electron densities during equinox are more



(a) Summer (Day 175)

(b) Equinox (Day 267)

(c) Winter (Day 358)



(d) Summer (Day 175)

(e) Equinox (Day 267)

(f) Winter (Day 358)

Figure 28. (Top row) Vertical TEC values at 0000 UT obtained from the IFM for different seasons during solar maximum (F10.7 = 225) and quiet geomagnetic conditions (Kp = 1). The TEC scale on the right-hand side of each panel ranges from 0 to 150 TECU. (Bottom row) Seasonal comparison of slant TEC differences at a GPS ground station located 8 degrees south of the geomagnetic equator in the Asian region during solar maximum (F10.7 = 225) and quiet geomagnetic conditions (Kp = 1).

concentrated along the geomagnetic equator where the plasma bubbles form, the slant TEC differences are greater compared to the other seasons.

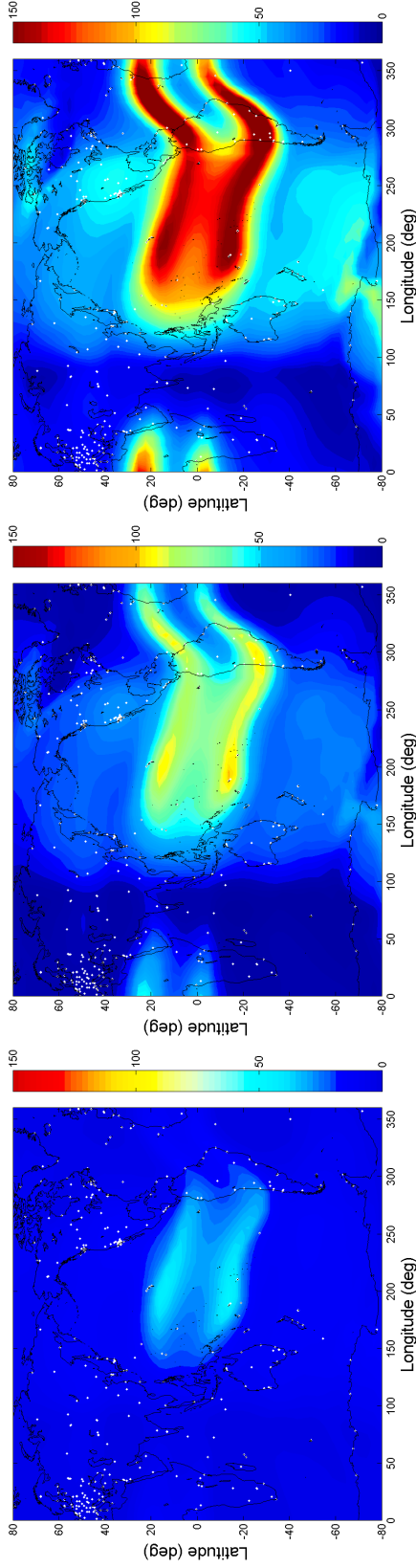
4.2.3 Solar Activity

An evaluation of slant TEC differences for different levels of solar activity is presented in Figure 29. The vertical TEC distributions for different levels of solar activity during equinox and quiet geomagnetic activity are presented in panels (a-c). The three panels correspond with F10.7 indices of 75, 150 and 225 solar flux units (SFU). The F10.7 index is a measure of the 10.7 cm solar radio flux and related to different levels of solar activity with 75 and 225 SFUs representing solar minimum and maximum conditions, respectively. Because the F10.7 index is related to the rate of photoionization in Earth's ionosphere, higher levels of solar activity will produce greater electron densities.

The slant TEC analysis results for different bubble configurations at a GPS ground station located at the geomagnetic equator in the African region during equinox and quiet geomagnetic conditions are shown in panels (d-f) of Figure 29. The three panels correspond to the same F10.7 indices in panels (a-c). The figure indicates that slant TEC differences are greatest during solar maximum in panel (f) compared to solar minimum in panel (d). Because solar maximum produced the greatest electron densities, solar maximum resulted in the greatest slant TEC differences.

4.2.4 Geomagnetic Activity

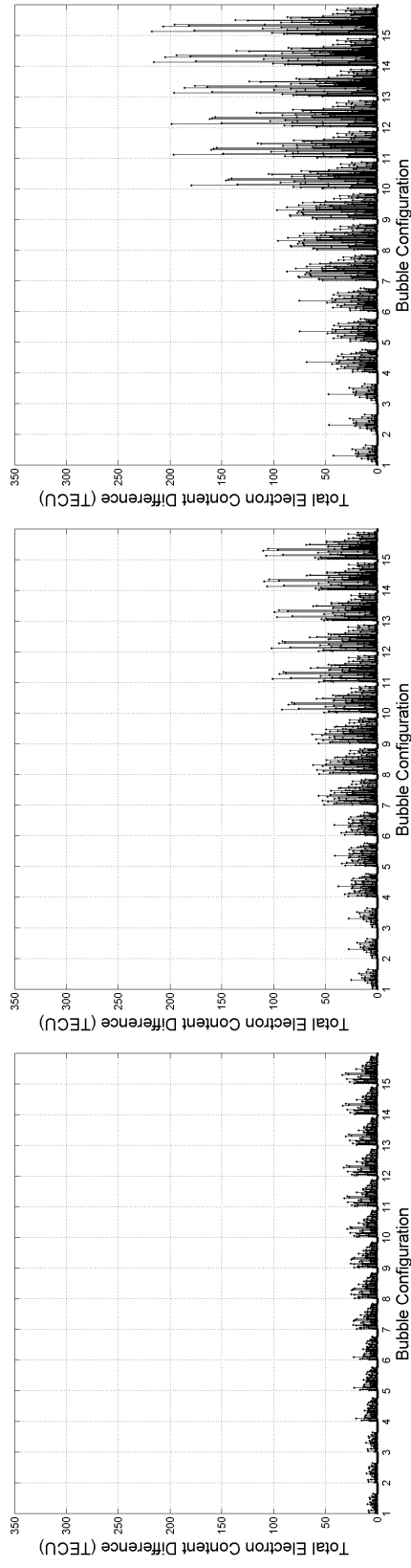
Vertical TEC values are plotted as a function of latitude and longitude at 0000 UT during solar maximum conditions at equinox in Figure 30 for different levels of geomagnetic activity. The figure consists of three panels, labeled (a-c), which range from quiet ($K_p = 1$) to extreme ($K_p = 9$) geomagnetic activity. The figure suggests



(a) F10.7 = 75 SFU

(b) F10.7 = 150 SFU

(c) F10.7 = 225 SFU

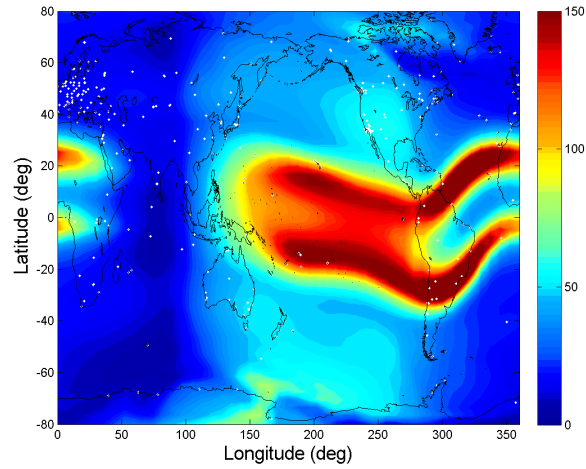


(d) F10.7 = 75 SFU

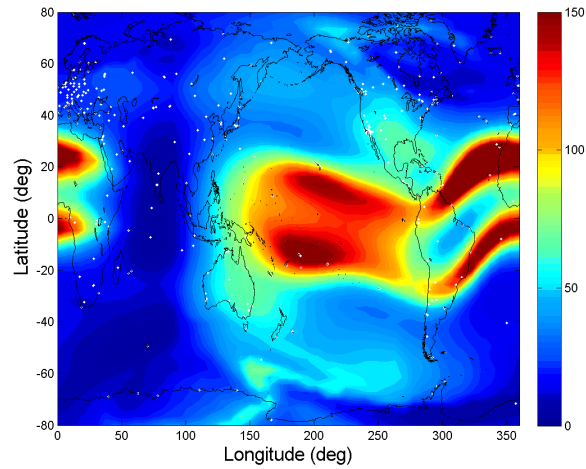
(e) F10.7 = 150 SFU

(f) F10.7 = 225 SFU

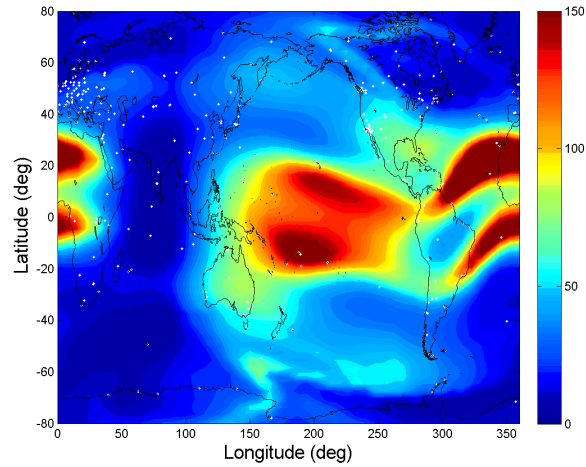
Figure 29. (Top row) Vertical TEC at 0000 UT obtained from the IFM for different levels of solar activity during equinox (Day 267) and quiet geomagnetic activity ($Kp = 1$). The TEC scale on the right-hand side of each panel ranges from 0 to 150 TECU. (Bottom row) Slant TEC difference obtained from the IFM as a function of solar activity for different bubble configurations at a GPS ground station located 8 degrees south of the geomagnetic equator in the Asian region at equinox (Day 267) during quiet geomagnetic activity ($Kp = 1$).



(a) $K_p = 1$



(b) $K_p = 5$



(c) $K_p = 9$

Figure 30. Vertical TEC at 0000 UT obtained from the IFM as a function of geomagnetic activity at equinox (Day 267) during solar maximum ($F_{10.7} = 225$).

that, depending on geographic location, vertical TEC will either increase or decrease with increased geomagnetic activity.

In order to investigate geographic TEC changes, slant TEC differences at two different GPS ground stations are plotted in Figure 31 during equinox and solar maximum conditions. Both GPS ground stations registered either an increase or decrease in slant TEC difference. The first GPS ground station, shown in panels (a) and (b), is located 16 degrees north of the geomagnetic equator in the African region, and indicates an increase in slant TEC difference when the geomagnetic activity level was raised to a Kp value of 9. In contrast, the second GPS ground station in panels (d) and (e), located 16 degrees south of the geomagnetic equator in the Atlantic region, displayed a decrease in slant TEC difference with increased geomagnetic activity.

In both figures, panels (c) and (f) show the vertical TEC difference between Kp = 9 and Kp = 1 as a function of geographic latitude and longitude, ranging from -75 to +75 TECU. Overall, the panels indicate that depending on geographic location, slant TEC differences will either increase or decrease with increased geomagnetic activity. During geomagnetic storming, the rapid expansion of the thermosphere produces pressure gradients that drive strong neutral winds that disturb the thermospheric circulation, altering the neutral composition of the atmosphere [1]. In addition, ionospheric plasma is moved up and down geomagnetic field lines, changing plasma production, recombination rates, electron densities and, hence, TEC [1].

This chapter presented the results of the look angle and slant TEC analyses. A copy of all results can be obtained by contacting the author or the Department of Engineering Physics at AFIT. The next chapter will discuss the results of both analyses and their use in computational and operational applications. Topics for further study will also be suggested.

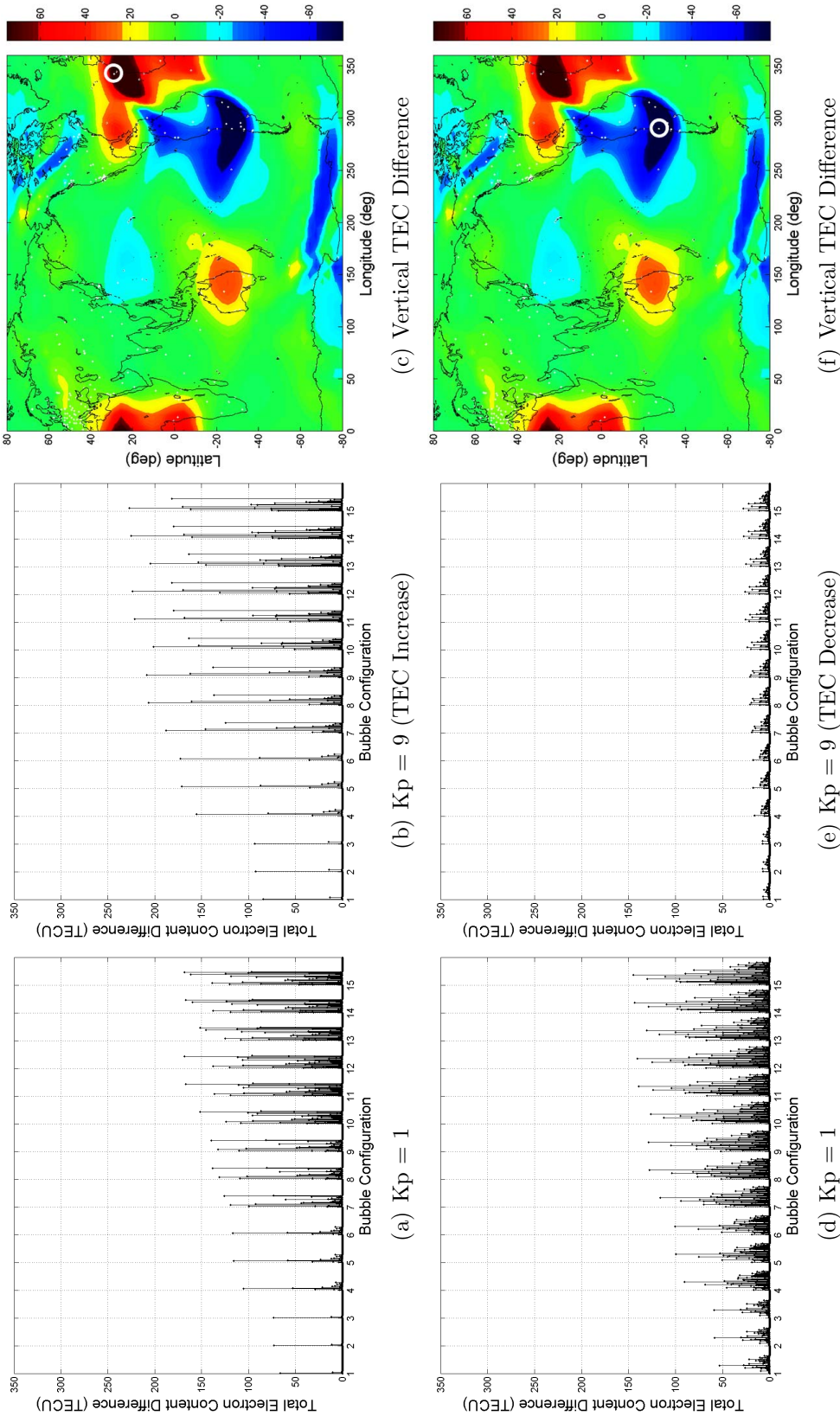


Figure 31. Slant TEC difference increase (a-b) and decrease (d-e) with increased geomagnetic activity at equinox (Day 267) during solar maximum (F10.7 = 225). Vertical TEC differences ($K_p = 9 - K_p = 1$) are shown in panels (c) and (f) at 0000 UT. The scale on the right side of the figure ranges from -75 TECU to +75 TECU. The respective GPS ground stations are circled in white.

V. Discussion

The results of the look angle and slant TEC analyses are discussed in this chapter, including their use in computational and operational applications. Afterwards, topics for further study will be suggested and the findings of the study will be summarized.

5.1 Look Angle Analysis

When using the look angle analysis results, it should be noted that several assumptions were made that will slightly alter the affected look angle profiles. First, it was assumed that the entire plasma bubble region was instantaneously depleted when created and filled when dissipated. Plasma bubbles have been observed to grow at different rates which will change how the affected look angles evolve. In addition, plasma bubbles do not always begin forming at exactly 2000 LT. As a result, GPS ground stations will see the plasma bubbles at different times which will deviate from the look angle analysis results. Lastly, the plasma bubbles were not allowed to drift to the east as noted in observations. The eastward drift will cause the plasma bubble profiles to become slightly skewed. To the east, affected elevation angles will slowly decrease over time as plasma bubbles move away from the GPS ground station while affected elevation angles to the west will increase as the bubbles approach the station.

The results of the look angle analysis will be beneficial for both operational and computational applications. Operationally, the look angle analysis results will indicate where and when scintillation will possibly affect communications and GPS-related operations. The results suggest that larger plasma bubbles will cause more radio and satellite communication problems. In addition, GPS ground stations located closer to the geomagnetic equator will be affected by more communication problems. Lastly, the time evolution results will enable military leaders to plan and

execute military operations with more success by knowing when radio and satellite communication problems due to plasma bubbles are expected to begin and end. When used in combination with the plasma bubble occurrence statistics detailed in the literature, the look angle analysis data can be applied at any time of the year and at any geographic location.

Computationally, the affected look angle profiles for each GPS ground station will only allow GPS satellite data uninfluenced by plasma bubbles to be assimilated into GAIM, increasing the accuracy of the model output. The results suggest that larger plasma bubbles will result in less model accuracy compared to smaller bubbles. Larger plasma bubbles will prevent more GPS ionospheric measurement data from being ingested into the model, resulting in a less accurate reconstruction of Earth's ionosphere. It is also expected that the modeled ionosphere near the geomagnetic equator will be less accurate than at farther distances since less GPS measurement data will be assimilated. In contrast, the look angle time evolution results will maximize the amount of ingested GPS data, increasing the overall accuracy of the GAIM model. Lastly, the results of the look angle analysis can also be used to alert GAIM model users that the reconstructed ionosphere at certain geographic locations may be suspect due to the presence of plasma bubbles.

5.2 Slant TEC Analysis

Because the slant TEC analysis was conducted using a physics-based model of the ionosphere, the results should be interpreted in terms of geophysical trends, instead of actual forecasted TEC measurements. The slant TEC calculations assumed the same depletion factor for the entire plasma bubble region. In reality, depletion factors will vary throughout the plasma bubble volume. Furthermore, the ionosphere and GPS satellite positions are constantly changing. Despite these factors, the ef-

fects of different geophysical conditions on slant TEC, and hence, radio and satellite communications will still be consistent with the results of the analysis.

The analysis results indicate that larger plasma bubbles, greater depletion extents, higher levels of solar activity and the equinoctial months will cause greater radio and satellite communication problems. In addition, it was discovered that slant TEC differences either increased or decreased depending on geographic location. Of all of the geophysical conditions, geomagnetic activity is the most important because of the spontaneity of geomagnetic storming. When combined with the look angle analysis results and plasma bubble occurrence statistics, military leaders will not only know when specific geographic locations will be affected, but the expected magnitude of radio and satellite communication problems for a wide range of geophysical conditions and plasma bubble configurations.

5.3 Further Study

Two topics of further study are suggested in this section that will create new opportunities to advance the knowledge of plasma bubbles and its application to the Air Force and Department of Defense.

5.3.1 Singapore University Research Collaboration

Since the country of Singapore is located nine degrees in latitude south of the geomagnetic equator, it is in a prime location to detect plasma bubbles of many different sizes. With access to a GPS ground station, dual-frequency GPS data and programs to calculate scintillation and slant TEC, a study can be conducted to compare the results of this research with observed plasma bubble measurements.

By plotting the calculated slant TEC values over time, a method can be used to locate the edges of plasma bubble depleted regions by detecting sudden changes in

TEC and amplitude scintillations using the S_4 index. Once a plasma bubble region is detected, affected look angles can be recorded by obtaining GPS position data and matching the observation times. By plotting the affected azimuth and elevation angles, the bubble size and structure can be estimated and compared with the results in this study. In addition, the slant TEC values can be used to determine the depletion extent of the plasma bubbles. Lastly, the affected look angles can be plotted over time to analyze the evolution of the plasma bubble structure. By comparing the theoretical and observed data, refinements to the plasma bubble structure and characteristics used in this study can be made.

It is important that the research be conducted during Singapore's plasma bubble season. According to the plasma bubble occurrence statistics in Figure 8, conducting the research during the upcoming solar maximum in 2013 at equinox will be the best opportunity to observe not only the most number of plasma bubbles, but the largest ones as well. This research collaboration will also be a great opportunity to open a new academic relationship between AFIT and Singapore University.

5.3.2 Scintillation Network Decision Aid (SCINDA) Data

Another study can be conducted using the Air Force Research Laboratory's (AFRL) Scintillation Network Decision Aid (SCINDA) data. SCINDA computes both scintillation (S_4 index) and TEC at a high sampling rate [2]. Once plasma bubble regions are detected, the TEC data and GPS satellite positions can be recorded to calculate the affected look angles. As a result, the plasma bubble structure and depletion extent can be estimated and compared with the bubble configurations used in this research. Unlike the Singapore University research collaboration, this study can be conducted globally, instead of locally. Using SCINDA GPS receiver stations around the world, the study can be conducted during any time of the year. Access to archived data can

also be helpful in consolidating plasma bubble occurrence statistics as a function of geographic position, solar activity, season and even geomagnetic activity level.

5.4 Conclusion

This research calculated affected look angles and TEC deviations due to plasma bubbles of various sizes for 27 geophysical conditions consisting of different seasons and levels of solar and geomagnetic activity at 421 GPS ground stations worldwide. The results of this research are important and will make a difference.

A plot of affected GPS ground stations for various plasma bubble sizes is shown in Figure 32. Because the data points overlay each other, the top data point indicates the smallest plasma bubble detected at the GPS ground station. Plasma bubbles of 3000 km base extent affect geographic locations near the geomagnetic equator. Larger plasma bubbles affect higher latitude locations. The figure provides a quick summary of geographic locations that can expect to experience some degree of radio and satellite communication disruption due plasma bubbles of various sizes. The stars indicate locations of U.S. military conflict, to include: Iraq, Afghanistan, Korea, Southern Philippines and Columbia. The results have reiterated many times; plasma bubbles are detrimental to military operations.

Overall, this research collaboration with Utah State University will improve the accuracy of the current and future operational ionospheric models at the Air Force Weather Agency, enhancing the Air Force's space weather forecasting capability. In addition, the results of this research will create an archive of information that can provide military leaders with a clear picture of the expected plasma bubble impacts to radio and satellite communications reliability when planning and executing military operations from the strategic to tactical level, inevitably contributing to mission success.

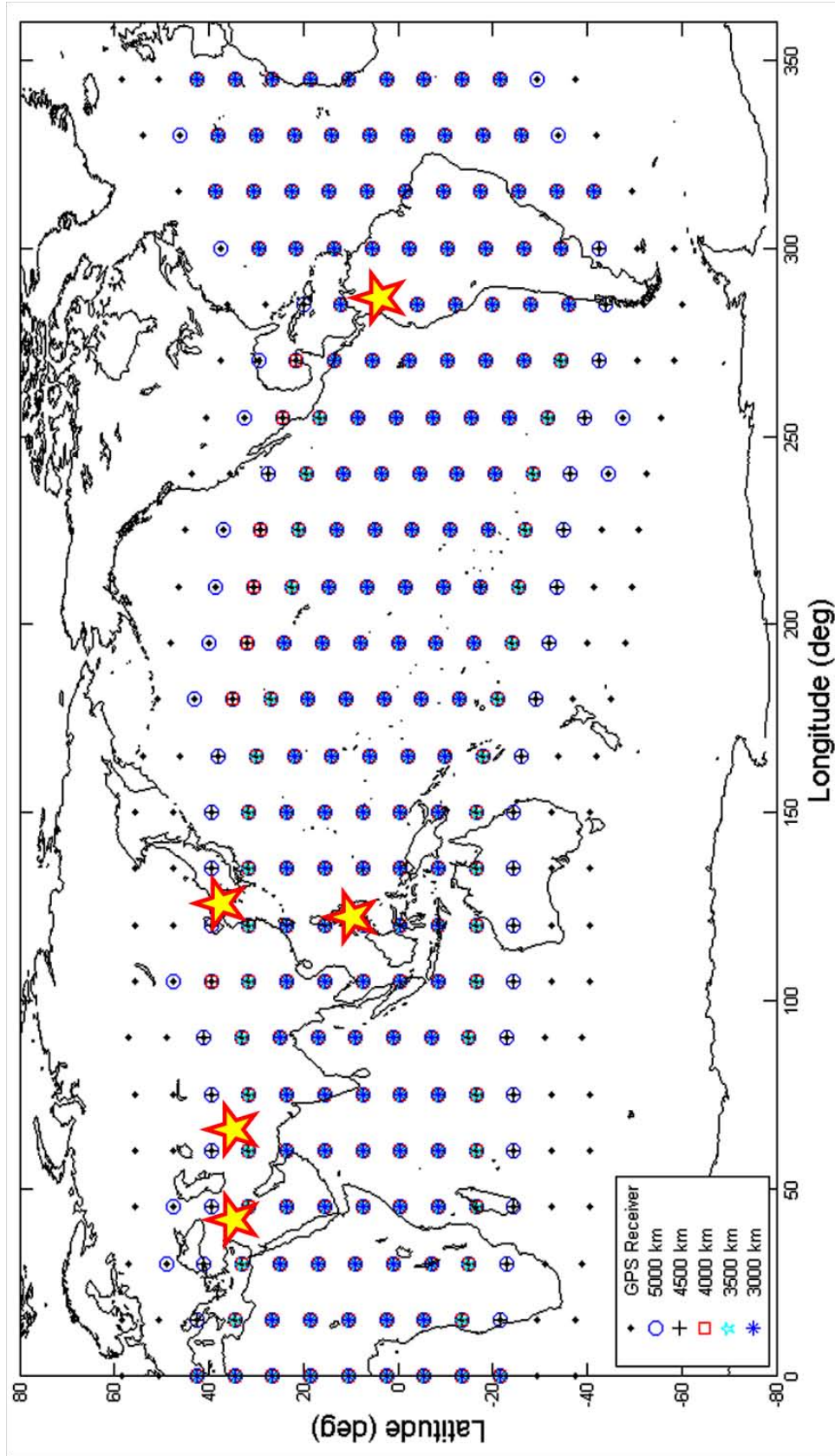


Figure 32. Affected GPS ground stations as a function of plasma bubble size over a period of 24 hours using the IDEAL grid. Because the data points overlay each other, the top data point indicates the smallest plasma bubble detected at the GPS ground station. The stars indicate locations of United States military conflict: Iraq, Afghanistan, Korea, Southern Philippines and Columbia.

Bibliography

- [1] Buonsanto, M.J. “Ionospheric Storms - A Review”. *Space Science Reviews*, 88:563–601, 1999.
- [2] Carrano, C.S. and K.M. Groves. “TEC Gradients and Fluctuations at Low Latitudes Measured with High Data Rate GPS Receivers”. *ION 63rd Annual Meeting*, 156–163. 2007.
- [3] Griffiths, J. “National Geodetic Survey Precise Orbits”. World Wide Web Page, 2010. 7 December 2010.
<http://www.ngs.noaa.gov/orbits/>.
- [4] Huang, C.Y., W.J. Burke, J.S. Machuzak, L.C. Gentile, and P.J. Sultan. “DMSP Observations of Equatorial Plasma Bubbles in the Topside Ionosphere Near Solar Maximum”. *Journal of Geophysical Research*, 106(A5):8131–8142, 2001.
- [5] IGS Central Bureau. “International GNSS Service”. World Wide Web Page, 2010. 7 December 2010.
<http://igsb.jpl.nasa.gov/>.
- [6] Kintner, P.M., B.M. Ledvina, and E.R. de Paula. “GPS and Ionospheric Scintillations”. *Space Weather*, 5, 2007.
- [7] Li, G., B. Ning, L. Liu, W. Wan, and J.Y. Liu. “Effect of Magnetic Activity on Plasma Bubbles Over Equatorial and Low-latitude Regions in East Asia”. *Annales Geophysicae*, 27:303–312, 2009.
- [8] Maruyama, T. “Ionosphere and Thermosphere”. *Journal of the Communications Research Laboratory*, 49(3):163–179, 2002.
- [9] Maus, S., S. Macmillan, S. McLean, B. Hamilton, A. Thomson, M. Nair, and C. Rollins. *The US/UK World Magnetic Model for 2010-2015*. Technical report, NOAA Technical Report NESDIS/NGDC, 2010.
- [10] Nishioka, M., A. Saito, and T. Tsugawa. “Occurrence Characteristics of Plasma Bubble Derived from Global Ground-based GPS Receiver Networks”. *Journal of Geophysical Research*, 113(A05301), 2008.
- [11] Noll, C.E. “CDDIS: NASA’s Archive of Space Geodesy Data”. World Wide Web Page, 2009. 7 December 2010.
http://cddis.gsfc.nasa.gov/gnss_datasum.html.
- [12] North Dakota Department of Transportation. “Training Manual For GPS Operations”. World Wide Web Page, 2008. 7 December 2010.
<http://www.dot.nd.gov/manuals/design/surveymanual/gps-operations.pdf>.

- [13] Ondoh, T. and K. Marubashi. *Science of Space Environment*. Ohmsha, Ltd, Japan, 2000.
- [14] Portillo, A., M. Herraiz, S.M. Radicella, and L. Ciralo. “Equatorial Plasma Bubbles Studied Using African Slant Total Electron Content Observations”. *Journal of Atmospheric and Solar-Terrestrial Physics*, 70:907–917, 2008.
- [15] Sahai, Y., P.R. Fagundes, and J.A. Bittencourt. “Transequatorial F-region Ionospheric Plasma Bubbles: Solar Cycle Effects”. *Journal of Atmospheric and Solar-Terrestrial Physics*, 62:1377–1383, 2000.
- [16] Satcom Online. “Calculate Azimuth And Elevation Angles”. World Wide Web Page, 2010. 7 December 2010.
<http://www.satcom.co.uk/article.asp?article=1>.
- [17] Schunk, R.W. and H.G. Demars. “Effect of Equatorial Plasma Bubbles on the Thermosphere”. *Journal of Geophysical Research*, 108(A6):1245–1252, 2003.
- [18] Schunk, R.W. and A.F. Nagy. *Ionospheres*. Cambridge University Press, New York, 2000.
- [19] Schunk, R.W., L. Scherliess, J.J. Sojka, D.C. Thompson, D.N. Anderson, M. Codrescu, C. Minter, T.J. Fuller-Rowell, R.A. Heelis, M. Hairston, and B.M. Howe. “Global Assimilation of Ionospheric Measurements (GAIM)”. *Radio Science*, 39, 2004.
- [20] Schunk, R.W., L. Scherliess, and D.C. Thompson. “Ionosphere Data Assimilation: Problems Associated with Missing Physics”, 2010.
- [21] Shiokawa, K., Y. Otsuka, T. Ogawa, and P. Wilkinson. “Time Evolution of High-Altitude Plasma Bubbles Imaged At Geomagnetic Conjugate Points”. *Annales Geophysicae*, 22:3137–3143, 2004.
- [22] Sinha, H.S.S. and S. Raizada. “Some New Features of Ionospheric Plasma Depletions Over the Indian Zone Using All Sky Optical Imaging”. *Earth Planets Space*, 52:549–559, 2000.
- [23] Tobiska, W.K. “New Space Weather Mitigation Capabilities”. *American Institute of Aeronautics and Astronautics*, 2009.

Vita

Captain Omar A. Nava graduated from Jesuit College Preparatory School in Dallas, Texas in 2001. He entered undergraduate studies at the United States Air Force Academy in Colorado Springs, Colorado where, in June 2005, he graduated with a Bachelor of Science degree in Physics and received his commission as a Second Lieutenant in the United States Air Force.

For his first assignment, Captain Nava was selected to attend the Naval Post-graduate School in Monterey, California through the Basic Meteorology Program. After graduating with a Bachelor of Science degree in Meteorology in June 2006, he was assigned to Scott Air Force Base in Belleville, Illinois as a Senior Duty Officer or Lead Meteorologist. In November 2008, Captain Nava was assigned to Osan Air Base, South Korea where he served as the Wing Weather Officer for the 51st Fighter Wing. After 10 months in South Korea, he was selected to enter the Graduate School of Engineering and Management at the Air Force Institute of Technology at Wright-Patterson Air Force Base, Ohio in October 2009. Upon graduation, he will be assigned to the 614th Air and Space Operations Center at Vandenberg Air Force Base as the Weather Specialty Team Flight Commander.

REPORT DOCUMENTATION PAGE

Form Approved
OMB No. 0704-0188

The public reporting burden for this collection of information is estimated to average 1 hour per response, including the time for reviewing instructions, searching existing data sources, gathering and maintaining the data needed, and completing and reviewing the collection of information. Send comments regarding this burden estimate or any other aspect of this collection of information, including suggestions for reducing this burden to Department of Defense, Washington Headquarters Services, Directorate for Information Operations and Reports (0704-0188), 1215 Jefferson Davis Highway, Suite 1204, Arlington, VA 22202-4302. Respondents should be aware that notwithstanding any other provision of law, no person shall be subject to any penalty for failing to comply with a collection of information if it does not display a currently valid OMB control number. **PLEASE DO NOT RETURN YOUR FORM TO THE ABOVE ADDRESS.**

1. REPORT DATE (DD-MM-YYYY) 24-03-2011		2. REPORT TYPE Master's Thesis		3. DATES COVERED (From — To) Jun 2010 — Mar 2011	
4. TITLE AND SUBTITLE Analysis of Plasma Bubble Signatures in the Ionosphere				5a. CONTRACT NUMBER	
				5b. GRANT NUMBER	
				5c. PROGRAM ELEMENT NUMBER	
6. AUTHOR(S) Omar A. Nava, Capt, USAF				5d. PROJECT NUMBER	
				5e. TASK NUMBER	
				5f. WORK UNIT NUMBER	
7. PERFORMING ORGANIZATION NAME(S) AND ADDRESS(ES) Air Force Institute of Technology Graduate School of Engineering and Management (AFIT/EN) 2950 Hobson Way WPAFB OH 45433-7765				8. PERFORMING ORGANIZATION REPORT NUMBER AFIT/GAP/ENP/11-M06	
9. SPONSORING / MONITORING AGENCY NAME(S) AND ADDRESS(ES) Center for Atmospheric Space Sciences Attn: Robert Schunk 4405 Old Main Hill, Room 246 LOGAN UT 84322-4405 CMCL: 435-797-2961 EMAIL: shawna@cc.usu.edu				10. SPONSOR/MONITOR'S ACRONYM(S) CASS, AFWA	
				11. SPONSOR/MONITOR'S REPORT NUMBER(S)	
12. DISTRIBUTION / AVAILABILITY STATEMENT APPROVED FOR PUBLIC RELEASE; DISTRIBUTION UNLIMITED.					
13. SUPPLEMENTARY NOTES					
14. ABSTRACT Plasma bubbles are large scale structures of depleted plasma density in Earth's ionosphere that disrupt radio and satellite communications, to include global navigation satellite systems. This study used the Ionospheric Forecast Model (IFM) to analyze affected look angles and total electron content (TEC) differences due to plasma bubbles of various sizes for 27 geophysical conditions consisting of different seasons and levels of solar and geomagnetic activity at 421 GPS ground stations worldwide. Overall, different geographic locations and plasma bubble configurations produced different affected look angle profiles. Bigger plasma bubbles, larger density depletion factors, higher levels of solar activity and the equinoctial months resulted in greater slant TEC differences and, hence, greater communication problems. The results of this study not only improved the accuracy of the Air Force's operational ionospheric model and space weather forecasting capability, but also provided military leaders with a clear picture of the expected plasma bubble impacts to communications reliability when planning and executing military operations from the strategic to tactical level.					
15. SUBJECT TERMS Plasma Bubble, Look Angle, GPS, IFM, GAIM					
16. SECURITY CLASSIFICATION OF:			17. LIMITATION OF ABSTRACT	18. NUMBER OF PAGES	19a. NAME OF RESPONSIBLE PERSON
a. REPORT	b. ABSTRACT	c. THIS PAGE			Dr. William F. Bailey, AFIT/ENP
U	U	U	U	81	19b. TELEPHONE NUMBER (include area code) (937) 255-3636, x4501; william.bailey@afit.edu